UNIVERSIDAD DE VIGO

Escuela Técnica Superior de Ingenieros Industriales de Vigo

Departamento de Diseño en la Ingeniería

PROYECTO FIN DE CARRERA

Unit Cell Based Evaluation of Strain Energy Densities in Transforming Three-Phase Materials

Alumno:
Alfonso Bartolomé Chavert

Director:
Ao.Univ.Prof. Dipl.-Ing. Dr.techn. Helmut Böhm

Vienna, Junio 2011

Contents

Acknowledgements

I would like to thank Ao.Univ.Prof. Dipl.-Ing. Dr.techn. Helmut Böhm for the supervision of my thesis. I am deeply indebted to him for his support and for his useful and challenging advice. Also, I want to thank Dr. Sergio Nogales for his help; although Juanitos' supporter, he is a great colleague and better person. Both of them have given me the opportunity to work for the Institute of Lightweight Design and Structural Biomechanics during the last stage of my thesis. Because of this, I will be always indebted to them.

I wish to acknowledge all colleagues at the ILSB for the kindness you have shown me and for the excellent working atmosphere at the institute.

Por último, quiero dar las gracias a mis padres y a mis hermanas por todo el apoyo recibido durante mis estudios, sobre todo en este último año.

Abstract

Over the past 25 years ternary hard coatings produced by chemical vapor deposition (CVD) have played an increasingly important role in many applications, e.g. in machining and in the automotive and aerospace industries. A group of important representatives of this class of material are titanium aluminium nitride (TiAlN) systems, which age harden at elevated temperatures due to spinodal decomposition of TiAlN into TiN and cubic AlN.

In order to describe the energetic balance and kinetics of the decomposition of supersaturated $Ti_{(1-x)}Al_xN$ the strain energy density (SED) associated with this transformation must be known. In the present work this SED is evaluated by treating the three-phase system as a composite consisting of two types of transforming particles (TiN, AlN) embedded in a matrix (TiAlN) or as a random three-phase material. Under these assumptions, the analytical and numerical methods of continuum micromechanics can be brought to bear on the problem, the emphasis being put on Finite-Element-based unit cell methods in the present case.

Cube-shaped volume elements consisting of a predefined number of periodic, non-overlapping, equally sized, spherical particles embedded in a matrix were generated by a Random Sequential Insertion technique. Periodicity boundary conditions were applied to these unit cells and the Finite Element Method (FEM) was used to obtain the elastic fields due to transformation strains prescribed to the particles. These fields, in turn, allowed evaluating the SED of the transformed system. Primarily, effects of the Al mole fraction, of the volume fractions of the particles and of the macroscopic constraints (unconstrained, fully constrained, layer-constrained) on the SED were studied. In addition, results were obtained for particles of polyhedral shape and for voxel-type random phase arrangements.

The predictions of the FEM-based periodic homogenization show that the SED is most strongly determined by the volume fraction of transformed material, by the Al mole fraction and by the microtopology of the volume elements used. In the case of matrix-inclusion topologies, the influence of the particle shape turned out to be rather small.

Excellent agreement with analytical Transformation Field Analysis models based on Mori-Tanaka methods was achieved when using matrix-inclusion microtopologies, thus verifying previous modeling work. This good agreement was traced to the low elastic contrast of the constituents of the TiAlN-TiN-AlN system.

V

Resumen

En los últimos 25 años, los recubrimientos ternarios endurecidos producidos mediante deposición química de vapor (CVD) han jugado un papel importante en numerosas aplicaciones, como por ejemplo en los procesos de mecanizado o en las industrias automovilística y aeroespacial. Los sistemas titanio aluminio nitrógeno (TiAlN) son un grupo representativo de esta clase de material, teniendo como característica principal el endurecimiento a altas temperaturas por efecto de la descomposición espinodal del TiAlN en TiN y AlN cúbico.

Para describir el balance energético y la cinemática de la descomposición del $Ti_{(1-x)}Al_xN$ supersaturado se debe conocer la densidad energética de deformación (SED) asociada a la transformación. En este trabajo la SED se evalua suponiendo el sistema trifásico como un compuesto formado por dos tipos de partículas incrustadas en una matriz (TiAlN) que sufren una transformación (TiN, AlN), o como un material trifásico con distribución aleatoria. Bajo esta hipótesis, los métodos analíticos y numéricos de la micromecánica continua se pueden emplear en el problema, enfatizando para el caso actual en el concepto de celda unitaria basada en el Método de Elementos Finitos (FEM).

Mediante una técnica de inserción aleatoria se generaron los elementos volumétricos de forma cúbica compuestos por un número predefinido de partículas esféricas, periódicas, de igual forma y tamaño, que no se solapan e incrustadas en una matriz. Condiciones de contorno periódicas fueron aplicadas a estas celdas unitarias y el FEM fue usado para obtener los campos elásticos causados por las deformaciones de transformación inducidas en las partículas. Estos campos, a su vez, permitieron la evaluación de la SED del sistema transformado. En primer lugar se estudiaron los efectos que la fracción molar de Al, la fracción volumétrica de las partículas y las restricciones macroscópicas (no restringido, totalmente restringido, restricción de capa) tenían en la SED. Además, los resultados se obtuvieron para partículas con formas poliédricas y para distribuciones aleatorias de vóxels.

Las predicciones del FEM muestran que la SED tiene una fuerte dependencia con la fracción volumétrica del material que sufre la transformación, con la fracción molar de Al y con la microtopología de los elementos volumétricos usados. En el caso de topologías matriz-inclusión, la influencia de la forma resultó ser bastante pequeña.

Se obtuvieron coincidencias muy buenas al comparar los resultados con el modelo analítico de análisis del campo de transformación (TFA) basado en el método Mori-Tanaka (MTM), pero siempre y cuando se usen microtopologías del tipo matriz-inclusión. De esta forma, también se verifica el trabajo de modelado que se realizó. Se puede concluir que la causa de la buena concordancia entre los métodos analíticos y numéricos empleados es debida al bajo contraste elástico de los constituyentes del sistema TiAlN-TiN-AlN.

Contents

Palabras Clave:

Método de Elementos Finitos, Micromecánica Continua, Celda Unitaria, Recubrimientos Endurecidos, Densidad Energética de Transformación.

Notation

In this thesis Nye notation is used for the mechanical variables. Tensors of order 4, such as elasticity, compliance and concentration tensors, are written as 6×6 quasi-matrices, and stress-, as well as strain-, like tensors of order 2 as 6-(quasi-)vectors. These 6-vectors are connected to index notation by the relations

$$
\boldsymbol{\sigma} = \begin{pmatrix} \sigma(1) \\ \sigma(2) \\ \sigma(3) \\ \sigma(4) \\ \sigma(5) \\ \sigma(6) \end{pmatrix} = \begin{pmatrix} \sigma_{11} \\ \sigma_{22} \\ \sigma_{33} \\ \sigma_{12} \\ \sigma_{13} \\ \sigma_{23} \end{pmatrix} \qquad \boldsymbol{\varepsilon} = \begin{pmatrix} \varepsilon(1) \\ \varepsilon(2) \\ \varepsilon(3) \\ \varepsilon(4) \\ \varepsilon(5) \\ \varepsilon(6) \end{pmatrix} = \begin{pmatrix} \varepsilon_{11} \\ \varepsilon_{22} \\ \varepsilon_{33} \\ \gamma_{12} \\ \gamma_{13} \\ \gamma_{23} \end{pmatrix} \quad ,
$$

where $\gamma_{ij} = 2\varepsilon_{ij}$, $i \neq j$ are the shear angles [28].

Tensors up to rank four are represented with the following notation:

- Tensors of rank four: boldface uppercase Roman letters. Examples: $\mathbf{A}$, $\mathbf{B}$.

- Tensors of rank two: bold Greek lower case letters. Examples: $\boldsymbol{\varepsilon}$, $\boldsymbol{\sigma}$.

- Tensors of rank one: lowercase bold Roman letters. Examples: $\mathbf{c}$, $\mathbf{u}$.

- Scalars: lowercase or uppercase Italic letters or non-bold Greek lower case letters. Examples: c_{el}, W, ξ.

Constituents (phases) are denoted by superscripts, with (p) standing for a general phase, (m) for a matrix and (i) for inhomogeneities. Transposed vectors are indicated by a superscript T and effective properties are denoted by a superscript asterisk ($*$).

List of abbreviations

The following abbreviations are used through this thesis:

- BCs: boundary conditions

- FEM: Finite Element Method

- IVOL: volume associated with an integration point

- MTM: Mori-Tanaka method

- PMAs: Periodic Microfield Approaches

- RVE: representative volume element

- SED: strain energy density

- TFA: Transformation Field Analysis

1 Introduction

For the past twenty years, interest in new thin hard coating materials in industry has increased. Nowadays these materials play a very important role in industrial applications such as high speed machining or dry machining. One important family within hard coatings are metastable titanium aluminium nitride ($Ti_{(1-x)}Al_xN$) systems used as cutting tools due to their excellent behaviour at high temperatures (high hardness and wear resistance). At this point, it is necessary to understand how to tailor a hard coating in order to achieve the desired properties and how will it behave during operation.

The focus in the present work is the determination of the strain energy density (SED) of a family of composite hard coatings for several cases of study. This family is a three-phase system: titanium aluminium nitride, $Ti_{(1-x)}Al_xN$, which can contain Al mole fractions (x) between 0 and 1. It is treated as a composite consisting of a matrix (TiAlN) and two families of inhomogeneous inclusions (AlN and TiN). Under the assumption that continuum mechanics can be used for the nanoscale phase domains involved, the tools of micromechanics of materials can be used to evaluate the SED.

The strain energy density is an important factor in the transformation kinetics and energetic balance of the $Ti_{(1-x)}Al_xN$ system [23]. It represents the elastic energy stored due to the misfit between the parent phase and the transformed daughter phases. A correct knowledge of how some factors (macroscopic constraints, Al mole fraction, phase volume fractions, inclusions' shape, particle distribution or elastic contrast) affect the SED makes it possible to explain partly (other energetic contributions are obviously involved) the decomposition of $Ti_{(1-x)}Al_xN$ to form AlN and TiN phases [23]. Also, the results obtained via a numerical method, periodic homogenization using the Finite Element method (FEM), are compared with those obtained via an analytical method, transformation field analysis (TFA). This way, the performance and accuracy of the TFA can be evaluated for different configurations.

The finite element method is employed in this thesis to compute the SED of three-dimensional unit cells which are used to approximate a representative volume element of $Ti_{(1-x)}Al_xN$. In order for the unit cell to represent an infinite material, periodicity boundary conditions are applied to it.

Continuum micromechanics provides the necessary methods and tools (periodic microfield and unit cell methods, RVE, boundary conditions, etc.) to link macroscopic and microscopic fields and, thus, determining the effective properties of the composite material as well as strain energies.

Material parameters of the transformation of $Ti_{(1-x)}Al_xN$ into AlN and TiN evaluated by ab initio calculations by Mayrhofer's group [23] were used in the micromechanical models.

1.1 Literature Review

Many analytical micromechanics theories have been developed and published in the literature; among them Eshelby's theory [9], Mori–Tanaka methods [2, 25] and self-consistent schemes [14] have been used to describe the effective properties of composites. One of the main problems of these classical models are their limitations in taking into account factors like shapes and size distributions of the inclusions contained in the composite.

These methods are not directly applicable to systems with multiple transforming phases, but there is an analytical scheme that allows to calculate the energetic state and the macroscopic properties of such transforming systems: the Transformation Field Analysis [8]. This method in combination with the Mori-Tanaka and classical self consistent schemes can describe the behaviour of both matrix-inclusion and non-matrix-inclusion topologies.

The unit cell concept based on the Finite Element method (FE-based PMAs) provides the necessary flexibility for analyzing factors that analytical methods cannot take into account. There exist different works that use this approach in order to obtain the effective properties of inhomogeneous materials [6, 34, 35]. The effect of the size, the shape and the volume fraction of the inclusions contained in a heterogeneous medium has also been discussed in [20, 28, 31, 36].

It is important to mention that the goal of this thesis is not to calculate the effective properties of the of the TiN-AlN-TiAlN system; the main aim of the study lies on the stress and strain states produced after the transformation of this material into AlN and TiN has occurred, that are described by the strain energy density. Work has been done on the SED for two-phase systems [26] and for multiphase systems [5] but no literature is available on unit cell based evaluations of the energetics of this class of material.

1.2 Hard Coatings

The tool price is often a significant part in the manufacturing price of a product. Therefore, the longer the tool lifetime, the higher will be its productivity. Together with improvements in the tool materials, protective coatings have been developed. Their main feature is the protection of the tool by their high hardness and chemical resistance, and they tend to be relatively brittle and expensive, so they are not appropriate as bulk tool materials. Hence, the combination of bulk material and coating ensures optimal tool properties, reducing wear and extending the tool life [18].

When hard coatings are used at high temperatures, they require excellent thermal, chemical and mechanical properties. Their main properties are:

- High hardness and reasonable toughness

- Low thermal conductivity

- Controlled adhesion

- Minimum diffusion and low friction

- Thermal stability

- Oxidation and corrosion resistance

The development of hard protective coatings started in the 1970s with the chemical (CVD) and physical (PVD) vapor deposition techniques. Many PVD variants are in use today (magnetron sputtering, evaporation by laser, cathode arc, electron beam, etc.).

The most common hard coatings are based on transition metal nitrides (TiN, CrN), but in the past decade there has been an increase in multicomponent coatings (TiAlN), multilayer coatings (TiN/TiAlN) as well as carbon-based coatings (DLC).

1.2.1 Applications

Hard coatings have been developed mainly for cutting machining processes but they are also employed in the aerospace and automotive industries.

High hardness, low coefficient of friction, and resistance against high temperatures allows high speed machining (HSM) and dry machining without use of cooling-lubricating liquids. These properties make it possible to increase the lifetime of the surface on to which a hard coating was deposited and to maintain tool precision during its use.

Figure 1.2.1: Tool machine working under dry conditions [22].

Hard coatings are also used on moving parts. Typical automotive and aerospace applications are parts of jet engines and car motors (engine valve system, gears, transmission system, etc.).

2 Theoretical Approach

In this chapter a short introduction into continuum micromechanics of materials is given. The theoretical approach is an extract of Böhm [4, 5], where further information can be found. Special emphasis is placed on the transformation field analysis and the concept of strain energy density; both of them play a significant role in the development of this thesis. Another important topic is the energetics of the phase transition of $\text{Ti}_{(1-x)}\text{Al}_x\text{N}$, which is explained in chapter 3.1.

2.1 Introduction

2.1.1 Inhomogeneous Materials

Many industrial and engineering materials as well as the majority of biological materials are inhomogeneous, i.e., they consist of dissimilar constituents that are distinguishable at some length scale. Each constituent shows different material properties and/or material orientations and may itself be inhomogeneous at some smaller length scale(s). Well-known examples of such materials are composites, concrete, polycrystalline materials, porous and cellular materials, functionally graded materials, wood, and bone.

An important aim of theoretical studies of multi-phase materials lies in deducing their overall ("effective" or "apparent") behavior from the corresponding material behavior of the constituents and from the geometrical arrangement of the phases.

The most basic classification criterion for inhomogeneous materials is based on the microscopic phase topology. In matrix–inclusion arrangements only the matrix shows a connected topology and the constituents play clearly distinct roles. In interpenetrating and random phase arrangements, in contrast, the phases cannot be readily distinguished topologically. Obviously, an important parameter in continuum micromechanics is the level of inhomogeneity of the constituents, which is often described by the phase contrast. For example, the elastic phase contrast takes the form

$$c_{\text{el}} = \frac{E^{(\text{i})}}{E^{(\text{m})}} \qquad , \tag{2.1.1}$$

where E stands for the Young's modulus, (m) denotes the matrix and (i) the inhomogeneities.

2.1.2 Length Scales

In the present context the lowest length scale described by a model is termed the microscale, the largest one the macroscale and intermediate ones are called mesoscales.

For each pair of length scales, on the one hand, the fluctuating contributions to the fields at the smaller length scale ("fast variables") influence the behavior at the larger length scale only via their volume averages. On the other hand, gradients of the fields as well as compositional gradients at the larger length scale ("slow variables") are not significant at the smaller length scale, where these fields appear to be locally constant and can be described in terms of uniform "applied fields" or "far fields". Formally, this splitting of the strain and stress fields, $\boldsymbol{\varepsilon}(\mathbf{r})$ and $\boldsymbol{\sigma}(\mathbf{r})$, into slow and fast contributions can be written as

$$\boldsymbol{\varepsilon}(\mathbf{r}) = \langle \boldsymbol{\varepsilon} \rangle + \boldsymbol{\varepsilon}^{'}(\mathbf{r}) \qquad \text{and} \qquad \boldsymbol{\sigma}(\mathbf{r}) = \langle \boldsymbol{\sigma} \rangle + \boldsymbol{\sigma}^{'}(\mathbf{r}) \qquad , \qquad (2.1.2)$$

where $\langle \boldsymbol{\varepsilon} \rangle$ and $\langle \boldsymbol{\sigma} \rangle$ are the macroscopic (slow) fields, whereas $\boldsymbol{\varepsilon}^{'}$ and $\boldsymbol{\sigma}^{'}$ stand for the microscopic fluctuations.

2.1.3 Homogenization and Localization

The "bridging of length scales", which constitutes the central issue of continuum micromechanics, involves two main tasks: homogenization and localization.

Homogenization may be interpreted as describing the behavior of a material that is inhomogeneous at some lower length scale in terms of an energetically equivalent, homogeneous reference material at some higher length scale. The local responses at the smaller length scale must be deduced from the loading conditions on the larger length scale; this task is referred to as localization.

For any volume element Ω_{s} of an inhomogeneous material that is sufficiently large and contains no significant gradients of composition or applied loads, homogenization relations take the form of volume averages of some variable $f(\mathbf{r})$,

$$\langle f \rangle = \frac{1}{\Omega_{\mathrm{s}}} \int_{\Omega_{\mathrm{s}}} f(\mathbf{r}) \mathrm{d}\Omega \qquad . \qquad (2.1.3)$$

Accordingly, the homogenization relations for the stress and strain tensors can be given as

$$\begin{aligned} \langle \boldsymbol{\varepsilon} \rangle &= \frac{1}{\Omega_{\mathrm{s}}} \int_{\Omega_{\mathrm{s}}} \boldsymbol{\varepsilon}(\mathbf{r}) \mathrm{d}\Omega \\ \langle \boldsymbol{\sigma} \rangle &= \frac{1}{\Omega_{\mathrm{s}}} \int_{\Omega_{\mathrm{s}}} \boldsymbol{\sigma}(\mathbf{r}) \mathrm{d}\Omega \qquad , \end{aligned} \qquad (2.1.4)$$

The microscopic strain and stress fields, $\boldsymbol{\varepsilon}(\mathbf{r})$ and $\boldsymbol{\sigma}(\mathbf{r})$, in a given volume element Ω_{s} are formally linked to the corresponding macroscopic responses, $\langle \boldsymbol{\varepsilon} \rangle$ and $\langle \boldsymbol{\sigma} \rangle$, by localization relations of the type

$$\boldsymbol{\varepsilon}(\mathbf{r}) = \mathbf{A}(\mathbf{r}) \langle \boldsymbol{\varepsilon} \rangle \qquad \text{and} \qquad \boldsymbol{\sigma}(\mathbf{r}) = \mathbf{B}(\mathbf{r}) \langle \boldsymbol{\sigma} \rangle \qquad . \qquad (2.1.5)$$

$\mathbf{A}(\mathbf{r})$ and $\mathbf{B}(\mathbf{r})$ are known as mechanical strain and stress concentration tensors, respectively. When they are known, localization tasks can obviously be carried out. Equations

(2.1.2) and (2.1.4) imply that the volume averages of fluctuations vanish for sufficiently large integration volumes,

$$\frac{1}{\Omega_{\mathrm{s}}} \int_{\Omega_{\mathrm{s}}} \boldsymbol{\varepsilon}^{'}(\mathbf{r}) \mathrm{d}\Omega = 0 = \frac{1}{\Omega_{\mathrm{s}}} \int_{\Omega_{\mathrm{s}}} \boldsymbol{\sigma}^{'}(\mathbf{r}) \mathrm{d}\Omega \quad . \qquad (2.1.6)$$

2.1.4 Volume Elements

Ideally, the homogenization volume should be chosen to be a proper representative volume element (RVE), i.e., a subvolume of Ω_{s} that is of sufficient size to contain all information necessary for describing the behavior of the composite. Representative volume elements can be defined, on the one hand, by requiring them to be statistically representative of the microgeometry. Such "geometrical RVEs" are independent of the physical property to be studied. On the other hand, the definition can be based on the requirement that the overall responses with respect to some given physical behavior are independent of the actual position and orientation of the RVE and/or of the boundary conditions applied to it ("physical RVEs").

An RVE must be sufficiently large to allow a meaningful sampling of the microfields and sufficiently small for the influence of macroscopic gradients to be negligible and for an analysis of the microfields to be possible [7, 13].

For RVEs the Hill condition [15] links the microscopic and macroscopic strain energy densities as

$$\frac{1}{2} \left\langle \boldsymbol{\sigma}^{\mathrm{T}} \boldsymbol{\varepsilon} \right\rangle = \frac{1}{2} \left\langle \boldsymbol{\sigma} \right\rangle^{\mathrm{T}} \left\langle \boldsymbol{\varepsilon} \right\rangle = \left\langle w \right\rangle \qquad (2.1.7)$$

i.e., strain energies can be evaluated from either microscopic and macroscopic fields.

2.1.5 Overall Behavior, Material Symmetries

The homogenized strain and stress fields of an elastic inhomogeneous material as obtained by equation (2.1.4), can be linked by effective elastic tensors $\mathbf{E}^{*}$ and $\mathbf{C}^{*}$ as

$$\left\langle \boldsymbol{\sigma} \right\rangle = \mathbf{E}^{*} \left\langle \boldsymbol{\varepsilon} \right\rangle \qquad \text{and} \qquad \left\langle \boldsymbol{\varepsilon} \right\rangle = \mathbf{C}^{*} \left\langle \boldsymbol{\sigma} \right\rangle \qquad , \qquad (2.1.8)$$

respectively, which may be viewed as the elastic tensors of an appropriate equivalent homogeneous material.

The resulting homogenized behavior of many multi-phase materials can be idealized as being statistically isotropic or quasi-isotropic. Statistically isotropic multi-phase materials show the same overall behavior in all directions, and their effective elasticity tensors and thermal expansion tensors take the form

$$
\mathbf{E} = \begin{pmatrix} E_{11} & E_{12} & E_{12} & 0 & 0 & 0 \\ E_{12} & E_{11} & E_{12} & 0 & 0 & 0 \\ E_{12} & E_{12} & E_{11} & 0 & 0 & 0 \\ 0 & 0 & 0 & E_{44} & 0 & 0 \\ 0 & 0 & 0 & 0 & E_{44} & 0 \\ 0 & 0 & 0 & 0 & 0 & E_{44} = \frac{1}{2}(E_{11} - E_{12}) \end{pmatrix} \qquad \boldsymbol{\alpha} = \begin{pmatrix} \alpha \\ \alpha \\ \alpha \\ 0 \\ 0 \\ 0 \end{pmatrix} \qquad (2.1.9)
$$

in Nye notation. Two independent parameters are sufficient for describing isotropic overall linear elastic behavior and one is required for the effective thermal expansion behavior in the linear range.

2.2 Major Modeling Strategies in Continuum Micromechanics of Materials

For convenience, the majority of the resulting modeling approaches may be treated as falling into two groups. The first of these comprises methods that describe interactions, e.g., between phases or between individual reinforcements, in a collective way in terms of phase-wise uniform fields and comprises

- Mean Field Approaches (MFAs) and related methods: The microfields within each constituent of an inhomogeneous material are approximated by their phase averages $\langle \boldsymbol{\varepsilon} \rangle^{(\mathrm{p})}$ and $\langle \boldsymbol{\sigma} \rangle^{(\mathrm{p})}$, i.e., piecewise uniform stress and strain fields are employed. The phase geometry enters these models via statistical descriptors, such as volume fractions, phase topology, reinforcement aspect ratio distributions, etc. In MFAs the localization relations take the form

$$
\begin{aligned}
\langle \boldsymbol{\varepsilon} \rangle^{(\mathrm{p})} &= \bar{\mathbf{A}}^{(\mathrm{p})} \langle \boldsymbol{\varepsilon} \rangle \\
\langle \boldsymbol{\sigma} \rangle^{(\mathrm{p})} &= \bar{\mathbf{B}}^{(\mathrm{p})} \langle \boldsymbol{\sigma} \rangle
\end{aligned}
\qquad (2.2.1)
$$

and the homogenization relations can be written as

$$
\begin{aligned}
\langle \boldsymbol{\varepsilon} \rangle^{(\mathrm{p})} &= \frac{1}{\Omega^{(\mathrm{p})}} \int_{\Omega^{(\mathrm{p})}} \boldsymbol{\varepsilon}(\mathbf{x}) \mathrm{d}\Omega \quad \text{with} \quad \langle \boldsymbol{\varepsilon} \rangle = \sum_{\mathrm{p}} \xi^{(\mathrm{p})} \langle \boldsymbol{\varepsilon} \rangle^{(\mathrm{p})} \\
\langle \boldsymbol{\sigma} \rangle^{(\mathrm{p})} &= \frac{1}{\Omega^{(\mathrm{p})}} \int_{\Omega^{(\mathrm{p})}} \boldsymbol{\sigma}(\mathbf{x}) \mathrm{d}\Omega \quad \text{with} \quad \langle \boldsymbol{\sigma} \rangle = \sum_{\mathrm{p}} \xi^{(\mathrm{p})} \langle \boldsymbol{\sigma} \rangle^{(\mathrm{p})}
\end{aligned}
\qquad (2.2.2)
$$

where $^{(\mathrm{p})}$ denotes a given phase of the material, $\Omega^{(\mathrm{p})}$ is the volume occupied by this phase and $\xi^{(\mathrm{p})} = \Omega^{(\mathrm{p})} / \sum_{\mathrm{k}} \Omega^{(\mathrm{k})}$ is the volume fraction of the phase. In contrast to equation (2.1.5) the phase concentration tensors $\bar{\mathbf{A}}$ and $\bar{\mathbf{B}}$ used in MFAs are not functions of the spatial coordinates. Mean field approaches tend to be formulated in terms of the phase concentration tensors, they pose low computational requirements, and they have been highly successful in describing the thermoelastic response of inhomogeneous materials.

- Variational Bounding Methods: Variational principles are used to obtain upper and lower bounds on the overall elastic tensors, elastic moduli, secant moduli, and other physical properties of inhomogeneous materials the microgeometries of which are described by statistical parameters. Bounds are important tools for assessing other models of inhomogeneous materials. Furthermore, in many cases one of the bounds provides good estimates for the physical property under consideration, even if the bounds are rather slack.

The second group of approximations is based on studying discrete microgeometries, for which they aim at fully accounting for the interactions between phases. It includes

- Periodic Microfield Approaches (PMAs), also referred to as periodic homogenization schemes or unit cell methods. In these methods the inhomogeneous material is approximated by an infinitely extended model material with a periodic phase arrangement. The resulting periodic microfields are usually evaluated by analyzing repeating unit cells via analytical or numerical methods. Unit cell methods are often used for performing materials characterization of inhomogeneous materials in the nonlinear range, but they can also be employed as micromechanically based constitutive models. The high resolution of the microfields provided by PMAs can be very useful for studying the initiation of damage at the microscale. However, because they inherently give rise to periodic configurations of damage and patterns of cracks, PMAs are not suited to investigating phenomena such as the interaction of the microgeometry with macroscopic cracks.
Periodic microfield approaches can give detailed information on the local stress and strain fields within a given unit cell, but they tend to be computationally expensive. All numerical models used in this thesis belong to this group of methods.

- Embedded Cell or Embedding Approaches: The inhomogeneous material is approximated by a model material consisting of a "core" containing a discrete phase arrangement that is embedded within some outer region to which far field loads are applied. The material properties of this outer region may be described by some macroscopic constitutive law, they can be determined self-consistently or quasi-self-consistently from the behavior of the core, or the embedding region may take the form of a coarse description and/or discretization of the phase arrangement. ECAs can be used for materials characterization, and they are usually the best choice for studying regions of special interest in inhomogeneous materials, such as the tips of macroscopic cracks and their surroundings. Like PMAs, embedded cell approaches can resolve local stress and strain fields in the core region at high detail, but tend to be computationally expensive, see, e.g., [39].

- Windowing Approaches: Subregions ("windows") are randomly chosen from a given phase arrangement and subjected to BCs that guarantee energy equivalence between the micro- and macroscales. Accordingly, windowing methods describe the behavior of individual inhomogeneous samples rather than of inhomogeneous materials and give rise to apparent rather than effective macroscopic responses [29].

2.3 Mean Field Methods

Mean field methods in continuum micromechanics aim at obtaining the overall properties of inhomogeneous materials, such as their overall elasticity and compliance tensors, $\mathbf{E}$ and $\mathbf{C}$, respectively, and their overall tensor of coefficients of thermal expansion (CTE), $\boldsymbol{\alpha}$, as well as descriptors related to phase transformations in terms of the appropiate phase properties and of statistical information on the phase topology and geometry. The descriptions are based on phase averaged stress and strain fields in the constituents, in terms of which localization is also carried out.

The most important mean field descriptions are:

- The Eshelby method for dilute composites.

- Mori-Tanaka approaches.

- Classical and generalized self-consistent schemes.

2.3.1 Transformation Field Analysis - Mori-Tanaka Method

Transformation field analysis (TFA) is a method for the micromechanical analysis of local fields and overall properties of multi-phase heterogeneous media subjected to uniform thermomechanical or transformation loading [8]. This approach relies on an explicit evaluation of piecewise uniform approximations of the residual fields that are introduced in multiphase solids by a distribution of piecewise uniform eigenstrains or eigenstresses (e.g. temperature changes, phase transformations), jointly referred to as transformation fields. When used with a suitable micromechanical model, in the present case with the Mori-Tanaka method (MTM) and the classic self consistent scheme (CSCS), the analysis provides piecewise uniform approximations of the local strain and stress fields in the phases, and estimates of the overall thermomechanical properties as well as the strain energy of a representative volume of the heterogeneous media.

In order to account for the presence of the different eigenstrains in the different constituents and for their interactions, this approach extends equations (2.2.1) to take the form

$$
\begin{aligned}
\langle \boldsymbol{\varepsilon} \rangle^{(\mathrm{p})} &= \bar{\mathbf{A}}^{(\mathrm{p})} \langle \boldsymbol{\varepsilon} \rangle + \sum \bar{\mathbf{D}}^{(\mathrm{pq})} \mathbf{e}^{(\mathrm{q})} \\
\langle \boldsymbol{\sigma} \rangle^{(\mathrm{p})} &= \bar{\mathbf{B}}^{(\mathrm{p})} \langle \sigma \rangle + \sum \bar{\mathbf{F}}^{(\mathrm{pq})} \mathbf{s}^{(\mathrm{q})}
\end{aligned}
\qquad , \qquad (2.3.1)
$$

and equations (2.1.5) to become

$$
\begin{aligned}
\langle \boldsymbol{\varepsilon} \rangle &= \mathbf{C}^{*} \langle \sigma \rangle + \mathbf{e}^{*} \\
\langle \boldsymbol{\sigma} \rangle &= \mathbf{E}^{*} \langle \boldsymbol{\varepsilon} \rangle + \mathbf{s}^{*}
\end{aligned}
\qquad . \qquad (2.3.2)
$$

The tensors $\bar{\mathbf{D}}^{(\mathrm{ij})}$ and $\bar{\mathbf{F}}^{(\mathrm{ij})}$ are referred to as the eigenstrain and eigenstress influence factor tensors.

With the above ansatz the overall stress and strain contributions, $\mathbf{e}^*$ and $\mathbf{s}^*$, due to the phase eigenstrains $\mathbf{e}^{(p)}$ and eigenstresses $\mathbf{s}^{(p)}$ can be expressed as

$$
\begin{aligned}
\mathbf{e}^* &= \sum_{(p)} \xi^{(p)} \left[\mathbf{e}^{(p)} - \sum \mathbf{C}^{(p)} \bar{\mathbf{F}}^{(pq)} \mathbf{E}^{(q)} \mathbf{e}^{(q)} \right] \\
\mathbf{s}^* &= \sum_{(p)} \xi^{(p)} \left[\mathbf{s}^{(p)} - \sum \mathbf{E}^{(p)} \bar{\mathbf{D}}^{(pq)} \mathbf{C}^{(q)} \mathbf{s}^{(q)} \right] \qquad .
\end{aligned}
\tag{2.3.3}
$$

By combining the TFA ansatz with the Mori-Tanaka expressions for the phase concentration tensors, strain influence tensors [8]

$$
\begin{aligned}
\bar{\mathbf{D}}_{\mathrm{M}}^{(mm)} &= \bar{\mathbf{A}}_{\mathrm{M}}^{(m)} \sum_{(j)\neq(m)} \xi^{(j)} (\mathbf{I} - \bar{\mathbf{A}}_{\mathrm{dil}}^{(j)})(\mathbf{E}^{(j)} - \mathbf{E}^{(m)})^{-1} \mathbf{E}^{(m)} \\
\bar{\mathbf{D}}_{\mathrm{M}}^{(im)} &= \bar{\mathbf{A}}_{\mathrm{M}}^{(i)} \sum_{(j)\neq(m)} \xi^{(j)} (\mathbf{I} - \bar{\mathbf{A}}_{\mathrm{dil}}^{(j)})(\mathbf{E}^{(j)} - \mathbf{E}^{(m)})^{-1} \mathbf{E}^{(m)} - (\mathbf{I} - \bar{\mathbf{A}}_{\mathrm{dil}}^{(i)})(\mathbf{E}^{(i)} - \mathbf{E}^{(m)})^{-1} \mathbf{E}^{(m)} \\
\bar{\mathbf{D}}_{\mathrm{M}}^{(mi)} &= -\xi^{(i)} \bar{\mathbf{A}}_{\mathrm{M}}^{(m)} (\mathbf{I} - \bar{\mathbf{A}}_{\mathrm{dil}}^{(i)})(\mathbf{E}^{(i)} - \mathbf{E}^{(m)})^{-1} \mathbf{E}^{(i)} \\
\bar{\mathbf{D}}_{\mathrm{M}}^{(ii)} &= (\mathbf{I} - \xi^{(i)} \bar{\mathbf{A}}_{\mathrm{M}}^{(i)})(\mathbf{I} - \bar{\mathbf{A}}_{\mathrm{dil}}^{(i)})(\mathbf{E}^{(i)} - \mathbf{E}^{(m)})^{-1} \mathbf{E}^{(i)} \\
\bar{\mathbf{D}}_{\mathrm{M}}^{(ij)} &= -\xi^{(j)} \bar{\mathbf{A}}_{\mathrm{M}}^{(i)} (\mathbf{I} - \bar{\mathbf{A}}_{\mathrm{dil}}^{(j)})(\mathbf{E}^{(j)} - \mathbf{E}^{(m)})^{-1} \mathbf{E}^{(j)}
\end{aligned}
\tag{2.3.4}
$$

and stress influence factor tensors

$$
\begin{aligned}
\bar{\mathbf{F}}_{\mathrm{M}}^{(mm)} &= \bar{\mathbf{B}}_{\mathrm{M}}^{(m)} \sum_{(j)\neq(m)} \xi^{(j)} (\mathbf{I} - \bar{\mathbf{B}}_{\mathrm{dil}}^{(j)})(\mathbf{C}^{(j)} - \mathbf{C}^{(m)})^{-1} \mathbf{C}^{(m)} \\
\bar{\mathbf{F}}_{\mathrm{M}}^{(im)} &= \bar{\mathbf{B}}_{\mathrm{M}}^{(i)} \sum_{(j)\neq(m)} \xi^{(j)} (\mathbf{I} - \bar{\mathbf{B}}_{\mathrm{dil}}^{(j)})(\mathbf{C}^{(j)} - \mathbf{C}^{(m)})^{-1} \mathbf{C}^{(m)} - (\mathbf{I} - \bar{\mathbf{B}}_{\mathrm{dil}}^{(i)})(\mathbf{C}^{(i)} - \mathbf{C}^{(m)})^{-1} \mathbf{C}^{(m)} \\
\bar{\mathbf{F}}_{\mathrm{M}}^{(mi)} &= -\xi^{(i)} \bar{\mathbf{B}}_{\mathrm{M}}^{(m)} (\mathbf{I} - \bar{\mathbf{B}}_{\mathrm{dil}}^{(i)})(\mathbf{C}^{(i)} - \mathbf{C}^{(m)})^{-1} \mathbf{C}^{(i)} \\
\bar{\mathbf{F}}_{\mathrm{M}}^{(ii)} &= (\mathbf{I} - \xi^{(i)} \bar{\mathbf{B}}_{\mathrm{M}}^{(i)})(\mathbf{I} - \bar{\mathbf{B}}_{\mathrm{dil}}^{(i)})(\mathbf{C}^{(i)} - \mathbf{C}^{(m)})^{-1} \mathbf{C}^{(i)} \\
\bar{\mathbf{F}}_{\mathrm{M}}^{(ij)} &= -\xi^{(j)} \bar{\mathbf{B}}_{\mathrm{M}}^{(i)} (\mathbf{I} - \bar{\mathbf{B}}_{\mathrm{dil}}^{(j)})(\mathbf{C}^{(j)} - \mathbf{C}^{(m)})^{-1} \mathbf{C}^{(j)}
\end{aligned}
\tag{2.3.5}
$$

can be obtained, where $(i), (j) \neq (m)$.

Like "standard" Mori-Tanaka methods, the TFA in the above form applies to matrix-inclusion topologies.

For phase topologies that are not of the matrix-inclusion type, the classical self-consistent scheme (also known as the two-phase self-consistent scheme) may be used to evaluate the dilute phase concentration tensors. Following [8] this leads to iterative TFA schemes of the type

$$\bar{\mathbf{A}}_{n+1}^{(p)} = \left[\mathbf{I} + \mathbf{S}_n \mathbf{C}_n (\mathbf{E}^{(p)} - \mathbf{E}_n)\right]^{-1}$$

$$\mathbf{E}_{n+1} = \sum_{(p)} \xi^{(p)} \mathbf{E}^{(p)} (\mathbf{I} - \sum_{(q)} \bar{\mathbf{D}}_{n+1}^{(pq)})$$

$$\bar{\mathbf{D}}_{n+1}^{(pp)} = (\mathbf{I} - \bar{\mathbf{A}}_{n+1}^{(p)})(\mathbf{E}^{(p)} - \mathbf{E}_n)^{-1}(\mathbf{I} - \xi^{(p)} \left[\bar{\mathbf{A}}_{n+1}^{(p)}\right]^T) \mathbf{E}^{(p)}$$

$$\bar{\mathbf{D}}_{n+1}^{(pq)} = -\xi^{(q)}(\mathbf{I} - \bar{\mathbf{A}}_{n+1}^{(p)})(\mathbf{E}^{(p)} - \mathbf{E}_n)^{-1} \left[\bar{\mathbf{A}}_{n+1}^{(q)}\right]^T \mathbf{E}^{(q)} \qquad (2.3.6)$$

and

$$\bar{\mathbf{B}}_{n+1}^{(p)} = \left[\mathbf{I} + \mathbf{E}_n(\mathbf{I} - \mathbf{S}_n)(\mathbf{C}^{(p)} - \mathbf{C}_n)\right]^{-1}$$

$$\mathbf{C}_{n+1} = \sum_{(p)} \xi^{(p)} \mathbf{C}^{(p)} (\mathbf{I} - \sum_{(q)} \bar{\mathbf{F}}_{n+1}^{(pq)})$$

$$\bar{\mathbf{F}}_{n+1}^{(pp)} = (\mathbf{I} - \bar{\mathbf{B}}_{n+1}^{(p)})(\mathbf{C}^{(p)} - \mathbf{C}_n)^{-1}(\mathbf{I} - \xi^{(p)} \left[\bar{\mathbf{B}}_{n+1}^{(p)}\right]^T) \mathbf{C}^{(p)}$$

$$\bar{\mathbf{F}}_{n+1}^{(pq)} = -\xi^{(q)}(\mathbf{I} - \bar{\mathbf{B}}_{n+1}^{(p)})(\mathbf{C}^{(p)} - \mathbf{C}_n)^{-1} \left[\bar{\mathbf{B}}_{n+1}^{(q)}\right]^T \mathbf{C}^{(q)} \qquad , \qquad (2.3.7)$$

where n is the iteration number. Obviously, some suitable starting solution must be provided for $n = 0$. The iterations are stopped when the norm of the difference between successive approximation to the effective elastic tensors falls below some specific limit.

Note that equations (2.3.4), (2.3.5), (2.3.6) and (2.3.7) cannot be used for homogeneous inclusions.

2.4 General Remarks on Modeling Approaches Based on Discrete Microstructures

Modeling approaches based on discrete microstructures trade off restrictions to the generality of the phase arrangements against the capability of using fine grained geometrical descriptions and of resolving details of the stress and strain fields at the length scale of the inhomogeneities. Because they describe the microfields in detail such approaches are often referred to as "full field methods". The main fields of application of these methods are studying the nonlinear behavior of inhomogeneous materials and evaluating the microscopic stress and strain fields of relevant microgeometries at high resolution.

There are two philosophies for obtaining heterogeneous volume elements for modeling: generating them by computer algorithms or basing them directly on geometries obtained by experiment.

Computer generated "synthetic" volume elements may be classified into two groups:

- Generic arrangements of a number of reinforcements that are randomly positioned and, where appropriate, randomly oriented [6, 13, 28, 31].

- Specific phase arrangements that have identical phase distribution statistics as some target material [38, 40].

For volume elements that contain considerable numbers of inhomogeneities or other microstructural features, statistically reconstructed phase arrangements are definitely more specific to a given target material than are generic random microgeometries.

Computer generated microgeometries have tended to employ idealized reinforcement shapes, equiaxed particles embedded in a matrix, for example, being often represented by spheres, and fibers by cylinders or prolate spheroids of appropriate aspect ratio.

Instead of generating phase arrangements by computer algorithms, volume elements may be chosen to follow as closely as possible the microgeometry in part of a given sample of the material to be modeled, obtained from metallographic sections, serial sections, tomographic data, etc. The resulting volume elements are often referred to as "real microstructure" models [3, 10].

The model geometry must be complex enough to capture the physical behavior of the material under study. A number of numerical studies [6, 41] have indicated that substantially larger volume elements may be necessary for satisfactorily approximating the required overall symmetry and for obtaining good agreement between the responses of statistically equivalent phase arrangements, especially at elevated overall inelastic strains. This indicates that the size of satisfactory multi-inclusion unit cells depends markedly on the phase material behavior.

At present, the FEM is the most popular numerical scheme for evaluating full field models, especially in the nonlinear range, where its flexibility and capability of supporting a wide range of constitutive descriptions for the constituents and for the interfaces between them are especially appreciated. An additional asset of the FEM in the context of continuum micromechanics is its ability to handle discontinuities in the stress and strain components (which typically occur at interfaces between different constituents) in a natural way via appropriately placed element boundaries.

Applications of the FEM to micromechanical studies tend to fall into four main groups, compare fig.2.4.1.

- Phase arrangements discretized by an often high number of "standard" continuum elements, the mesh being designed in such a way that element boundaries are positioned at all interfaces between constituents. Such approaches use unstructured meshes and have the advantage that in principle any microgeometry can be discretized at a prescribed resolution and that readily available commercial FE packages may be used. This approach is followed, e.g., in [6, 13, 21, 28, 34, 35, 36, 40].

- Special hybrid elements may be used, which are specifically formulated to model the deformation, stress, and strain fields in an inhomogeneous region consisting of a single inhomogeneity or void together with the surrounding matrix on the basis of some appropriate analytical theory, compare, e.g., [11].

- When the phase arrangements to be studied are based on digital images of actual microgeometries, structured meshes that consists of regular, rectangular or hexahedral elements of fixed size and have the same resolution as the digital data are

used. Such meshes have the advantage of allowing a straightforward automatic model generation from appropriate experimental data and of avoiding ambiguities in smoothing the digital data. This modeling strategy is followed, e.g., in [12, 37].

- Structured meshes may be combined with assigning phase properties at the integration point level of standard elements ("multi-phase elements"), for an example see [33].
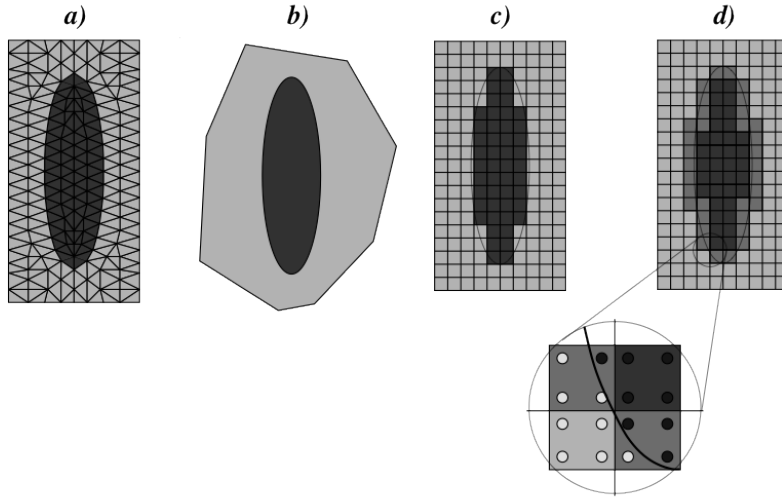

Figure 2.4.1: Sketch of FEM approaches used in micromechanics: a) discretization by standard elements, b) special hybrid elements, c) pixel/voxel discretization, d) "multi-phase elements" [4].

2.5 Periodic Microfield Models

Periodic Microfield Approaches (PMAs) aim at approximating the macroscopic and microscopic behavior of inhomogeneous materials by studying model materials that have periodic microstructures.

2.5.1 Basic Concepts of Unit Cell Models

Periodic microfield approaches analyze the behavior of infinite periodic phase arrangements under the action of far field mechanical loads, uniform temperature fields or transformation strains. The most common approach to studying the stress and strain fields in such periodic configurations is based on describing the microgeometry by a periodically repeating unit cell (RUC).

In periodic homogenization the strain and stress fields are decomposed into constant macroscopic strain and stress contributions ("slow variables"), $\langle \varepsilon \rangle$ and $\langle \sigma \rangle$, and periodically varying microscopic fluctuations ("fast variables"), $\varepsilon'(\mathbf{z})$ and $\sigma'(\mathbf{z})$, by analogy

13

to equation (2.5.1). Here $\mathbf{z}$ is a "microscopic coordinate" that has sufficient resolution for describing the variations on the microscale. The corresponding expression for the displacements takes the form

$$\mathbf{u}(\mathbf{z}) = \langle \varepsilon \rangle \, \mathbf{z} + \mathbf{u}'(\mathbf{z}) \qquad . \qquad (2.5.1)$$

In periodic microfield approaches each unit of periodicity (unit cell) contributes the same increment of the displacement vector $\Delta \mathbf{u}$ so that the homogenized displacements vary (multi)linearly. An idealized depiction of such a situation is presented in fig. 5.1, which shows the variations of the strains $\varepsilon_s(s) = \langle \varepsilon_s \rangle + \varepsilon'_s(s)$ and of the corresponding displacements $\mathbf{u}_s(s) = \langle \varepsilon_s \rangle \, s + \mathbf{u}'_s(s)$ along some line s in a hypothetical periodic two-phase material consisting of constituents A and B.
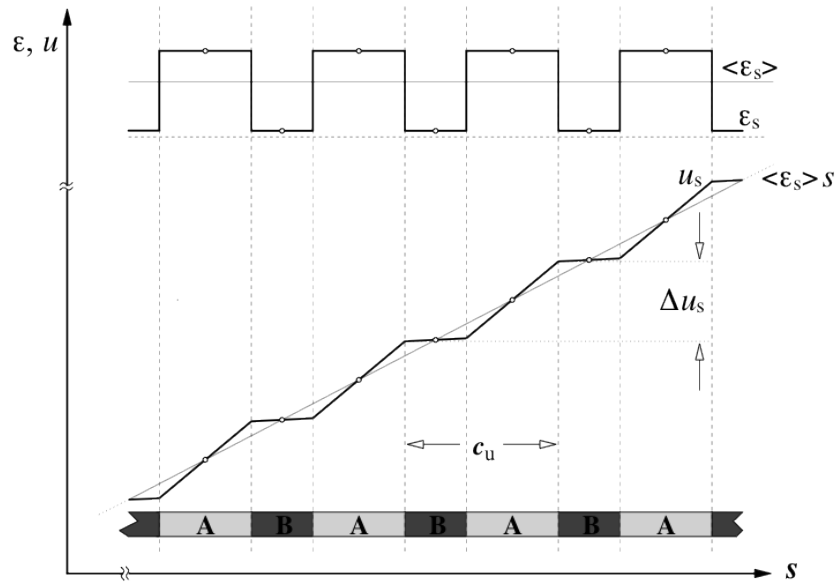
Figure 2.5.1: Schematic depiction of the variation of the strains $\varepsilon_s(s)$ and the displacements $\mathbf{u}_s(s)$ along a generic "one-dimensional composite" (coordinate s) consisting of constituents A and B. Symmetry points of $\varepsilon_s(s)$ and $\mathbf{u}_s(s)$ are indicated by small circles [4].

2.5.2 Boundary Conditions

Unit cells together with the boundary conditions (BCs) prescribed on them must generate valid tilings both for the undeformed geometry and for all deformed states pertinent to the problem. In order to achieve this, the BCs for the unit cells must be specified in such a way that all deformation modes appropriate for the load cases to be studied can be attained. The three major types of BCs used in periodic microfield analysis are periodicity, symmetry, and antisymmetry. Figure 2.5.2 shows some applications of

these types of boundary conditions for the case of a two-dimensional hexagonal array of inhomogeneities.
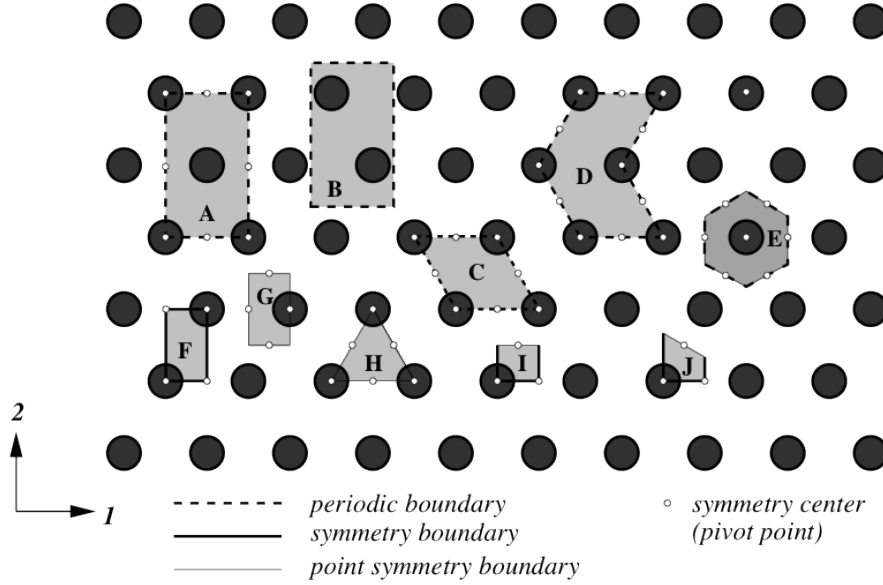

Figure 2.5.2: Periodic hexagonal array of circular inhomogeneities in a matrix and 10 unit cells that can be used to describe the mechanical responses of this arrangement under loads acting parallel to the coordinate axes [4].

The most general BCs for unit cells in continuum micromechanics are periodicity boundary conditions, which can handle any physically valid deformation state of the cell and, consequently, of the inhomogeneous material to be modeled.

The surface of any unit cell to be used with periodicity boundary conditions must consist of at least N pairs of faces (or pairs of parts of faces) Γ_k, and the surface elements making up a pair, k$-$ and k$+$, must be identical but shifted relative to each other by "shift vectors" $\mathbf{c}_k$ which are linear combinations of the periodicity vectors $\mathbf{p}_n$, $\mathbf{c}_k = \sum_l c_l^k \mathbf{p}_n$.

Figure 2.5.3 shows a two dimensional arrangement of inhomogeneities together with the periodicity vectors and a number of possible unit cells, all of which have the same volume.
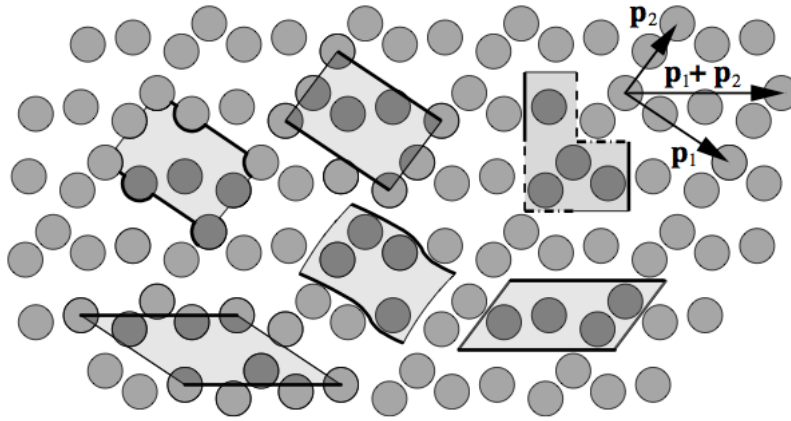
Figure 2.5.3: Six different but equivalent periodic minimum-size unit cells for a two-dimensional periodic matrix–inclusion medium with two (slightly) non-orthogonal translation vectors $\mathbf{p}_1$ and $\mathbf{p}_2$. Paired faces (or parts of faces) Γ_k are marked by identical line styles and regions belonging to one of the cells are highlighted by shading [4].
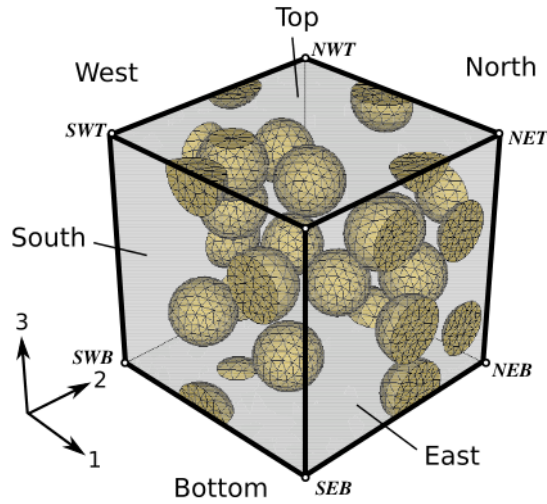

Figure 2.5.4: Cube-shaped periodic unit cell containing 15 randomly positioned spherical particles of equal size at a volume fraction of $\xi^{(i)} = 0.15$. Designators of the six faces (East, West, North, South, Top, Bottom) and of the vertices are given [29].

Because the unit cells tile the computational space by translation, neighboring cells must fit into each other in both undeformed and deformed states. For each pair of surface elements, Γ_k, equation (2.5.1) allows to express periodicity boundary conditions for the

mechanical problem in the small strain regime as

$$\Delta \mathbf{u}_k = \mathbf{u}_{k+} - \mathbf{u}_{k-} = \mathbf{u}(\mathbf{s}_k + \mathbf{c}_k) - \mathbf{u}(\mathbf{s}_k) = \langle \boldsymbol{\varepsilon} \rangle * \mathbf{c}_k \qquad , \qquad (2.5.2)$$

where $\mathbf{u}_{k+}$ and $\mathbf{u}_{k-}$ are the displacements at corresponding points $\mathbf{s}_k + \mathbf{c}_k$ and $\mathbf{s}_k$ of the surface elements k+ and k− (which may, e.g., correspond to faces N and S in figs.2.5.4 and 2.5.5), respectively. The $\mathbf{s}_k$ are position vectors on surface element k−, $\mathbf{s}_k + \mathbf{c}_k$ are the positions of the corresponding points on surface element k+, and $\langle \boldsymbol{\varepsilon} \rangle$ is the macroscopic strain, which is prescribed in displacement controlled analysis and must be determined in load controlled analysis. These conditions enforce a "seamless fit" between neighboring unit cells for all possible deformed states.
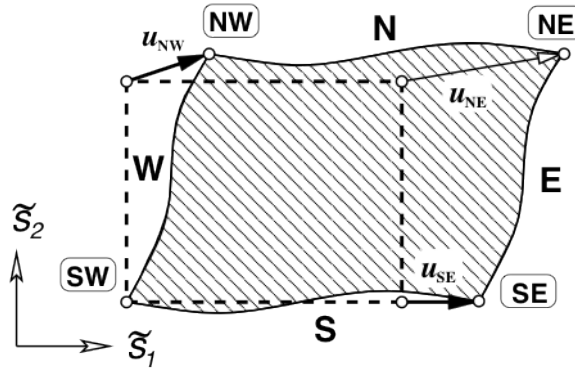
Figure 2.5.5: Sketch of periodicity boundary conditions as used with an initially rectangular two-dimensional unit cell [4].

2.5.2.1 Macroscopic Constraints

To obtain both phase strains and phase stresses for given constraint conditions, appropriate macroscopic strains and stresses must be used in equations (2.2.1) and (2.3.1).

For the macroscopically unconstrained case the overall stresses vanish (i.e., zero traction boundary conditions pertain), but there are in general nonzero overall strains, leading to the conditions

$$\begin{aligned} \langle \varepsilon \rangle &= \mathbf{e}^* \\ \langle \sigma \rangle &= \mathbf{0}. \end{aligned} \qquad (2.5.3)$$

In the macroscopically fully constrained case the effective strains are zero (i.e., zero strain boundary conditions prevail), but nonzero macrostresses are present. Accordingly the relations

$$\begin{aligned} \langle \varepsilon \rangle &= \mathbf{0} \\ \langle \sigma \rangle &= \mathbf{s}^*. \end{aligned} \qquad (2.5.4)$$

hold.

For thin layers that are perfectly bonded to a much stiffer substrate (such as thin coatings), the overall strains must be approximately zero in the plane of the layer (taken to be the 2-3 plane in the following), whereas the macroscopic stresses vanish in the normal direction (taken to be the 1-direction). For materials with transversely isotropic or higher effective symmetry the macroscopic strain and stress tensors corresponding to such conditions can be expressed as

$$
\begin{aligned}
\langle \varepsilon \rangle &= (e_{11}^* + a e_{22}^* + b e_{33}^*, 0, 0, e_{12}^*, 0, e_{31}^*)^\mathrm{T} \\
\langle \sigma \rangle &= (0, s_{22}^* - a s_{11}^*, s_{33}^* - b s_{11}^*, 0, s_{23}^*, 0)^\mathrm{T}
\end{aligned}
\tag{2.5.5}
$$

where a and b are defined as

$$
a = \frac{E_{1122}^*}{E_{1111}^*} \quad \text{and} \quad b = \frac{E_{1133}^*}{E_{1111}^*}
\tag{2.5.6}
$$

For materials with lower macroscopic symmetry more complex expressions may result. Note that the use of a micromechanical description implies that the layer's thickness must be at least an order of magnitude larger than the characteristic size of the inhomogeneities.

In equations (2.5.3) to (2.5.5), of each pair of macroscopic strain and stress components at least one vanishes. In general cases of prescribed far-field stresses and strains, equation (2.3.1) must be applied to evaluate the corresponding macroscopic strain and stress components, respectively, and the above property is lost.

2.5.3 Application of Loads and Evaluation of Fields

Once suitable unit cells have been defined and appropriate BCs applied, the volume elements must be subjected to appropriate loads in the form of uniform macroscopic stresses as well as strains, homogeneous temperature excursions, or suitable transformation strains, i.e., the microscopic and macroscopic fields must be linked.

The method of macroscopic degrees of freedom consists in applying far field stresses and strains to a given unit cell via concentrated nodal forces or prescribed displacements, respectively, at the master nodes and/or pivot points. The displacements or reaction forces at the master nodes, in turn, can be used to evaluate the macroscopic strains and stresses acting on the composite.

In order to obtain three-dimensional homogenized elastic tensors with the method of macroscopic degrees of freedom six suitable, linearly independent load cases must be solved for.

2.6 Strain Energy Density

The strain energy density is an important factor in the energetics of phase transformations, which play a major role in many industrially relevant processes in materials engineering.

The elastic strain energy of a volume Ω can be written as

$$W_{\mathrm{e}} = \frac{1}{2} \int_{\Omega} \boldsymbol{\sigma}^{\mathrm{T}}(\mathbf{r}) \boldsymbol{\varepsilon}_{\mathrm{e}}(\mathbf{r}) \mathrm{d}\Omega \qquad , \tag{2.6.1}$$

where $\boldsymbol{\varepsilon}_{\mathrm{e}}$ stands for the elastic strain.

For inhomogeneous materials consisting of constituents (p) of volume $\Omega^{(\mathrm{p})}$ (with $\sum_{(\mathrm{p})} \Omega^{(\mathrm{p})} = \Omega$) that take the form of a matrix (m) and inhomogeneities (i), where the latter (but not the former) are loaded by phase-wise homogeneous stress-free eigenstrains $\mathbf{e}^{(\mathrm{i})}$, equation (2.6.1) takes the form

$$W_{\mathrm{e}} = \frac{1}{2} \Omega \left\langle \boldsymbol{\sigma}^{\mathrm{T}} \boldsymbol{\varepsilon} \right\rangle - \frac{1}{2} \sum_{(\mathrm{i})} \Omega^{(\mathrm{i})} \left\langle \boldsymbol{\sigma} \right\rangle^{(\mathrm{i})\mathrm{T}} \mathbf{e}^{(\mathrm{i})} \qquad . \tag{2.6.2}$$

Assuming Ω to be a representative volume element, so that the Hill's condition, $\left\langle \boldsymbol{\sigma}^{\mathrm{T}} \boldsymbol{\varepsilon} \right\rangle = \left\langle \boldsymbol{\sigma} \right\rangle^{\mathrm{T}} \left\langle \boldsymbol{\varepsilon} \right\rangle$, holds, the elastic strain energy density of the material, $\left\langle w_{\mathrm{e}} \right\rangle = W_{\mathrm{e}}/\Omega$, results as

$$\left\langle w_{\mathrm{e}} \right\rangle = \frac{1}{2} \left\langle \boldsymbol{\sigma} \right\rangle^{\mathrm{T}} \left\langle \boldsymbol{\varepsilon} \right\rangle - \frac{1}{2} \sum_{(\mathrm{i}) \neq (\mathrm{m})} \xi^{(\mathrm{i})} \left\langle \boldsymbol{\sigma} \right\rangle^{(\mathrm{i})\mathrm{T}} \mathbf{e}^{(\mathrm{i})} \qquad . \tag{2.6.3}$$

Provided the macroscopic stresses and strains fulfill the condition $\left\langle \boldsymbol{\sigma} \right\rangle^{\mathrm{T}} \left\langle \boldsymbol{\varepsilon} \right\rangle = 0$, equation (2.6.3) allows the elastic strain energy density to be extended as

$$\left\langle w_{\mathrm{e}} \right\rangle = -\frac{1}{2} \sum_{(\mathrm{i}) \neq (\mathrm{m})} \xi^{(\mathrm{i})} \left\langle \boldsymbol{\sigma} \right\rangle^{(\mathrm{i})\mathrm{T}} \mathbf{e}^{(\mathrm{i})} \qquad . \tag{2.6.4}$$

This is the case for the three sets of constraints introduced in section 2.5.2.1.

Equations (2.6.3) and (2.6.4) can be evaluated by using estimates for the stresses in the inhomogeneities, $\left\langle \boldsymbol{\sigma} \right\rangle^{(\mathrm{i})}$, and, where required, for the macrofields $\left\langle \boldsymbol{\sigma} \right\rangle$ and $\left\langle \boldsymbol{\varepsilon} \right\rangle$ obtained with the TFA or with unit cell methods.

3 Modeling

This chapter describes the modeling process and general considerations assumed. Unit cell geometry and topology, element type employed, macroscopic constraints applied, loading cases and material properties are the main steps to define a periodic microfield model using the finite element method. Furthermore, micromechanical concepts such as length scales or periodicity of the unit cell are also taken into account.

3.1 Material Description: $Ti_{(1-x)}Al_xN$

Titanium aluminium nitride (TiAlN) or aluminium titanium nitride (AlTiN for Al mole fraction $x > 0.5$) is a metastable three-phase hard coating consisting of aluminium, titanium (metallic elements) and nitrogen (non-metallic element). As the Al mole fraction can vary between 0 and 1 the following expression is used: $Ti_{(1-x)}Al_xN$.

During annealing, structural changes occur in the coating, which transforms from a single-phase solid solution to a nanostructured three phase material by spinodal decomposition. These give rise to two different types of inhomogeneous phases (TiN and AlN) and an increase in hardness.

Another important point in the description of this material is the energetic balance during the decomposition process of $Ti_{(1-x)}Al_xN$ to form TiN and AlN precipitates. The energetic balance can be expressed depending on the volume fraction of transformed material ξ, the difference in chemical energy ΔG_{chem}, the elastic strain energy W_e and the interface energy O, as:

$$\Delta G = (\Delta G_{chem} - W_e - O)\xi \qquad . \qquad (3.1.1)$$

In the following the microstructure of this material is idealized, either, as a matrix-inclusion or as a random topology, although atom-probe investigations [22] have shown that these materials are heterogeneous at the nanoscale, where their phase topology is interpenetrating (figures 3.1.1 and 3.1.2).
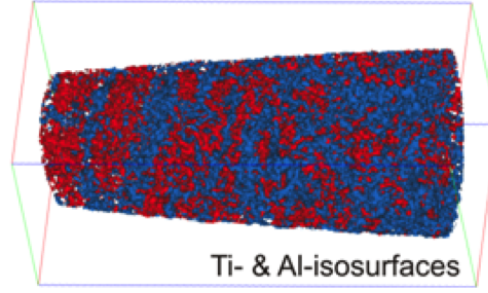
Figure 3.1.1: Microstructure sample of $Ti_{0.5}Al_{0.5}N$ obtained by 3D atom probe investigations [22]. Red phase represents Ti-isosurface and blue phase Al-isosurface. The total length of the sample is 30 nm.
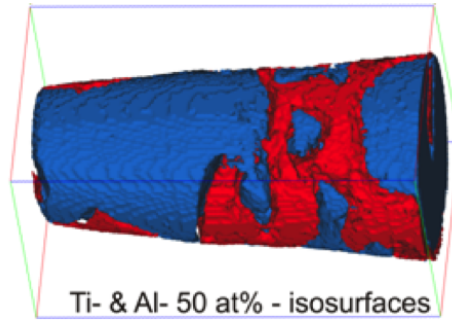

Figure 3.1.2: Microstructure sample of $Ti_{0.5}Al_{0.5}N$ obtained by 3D atom probe investigations [22]. Red phase represents Ti-isosurface and blue phase Al-isosurface.

Further explanations about microstructure, kinetics and energy balance of $Ti_{(1-x)}Al_xN$ can be found in [23].

The following relations link the volume fractions of the phases and the Al mole fraction x [5]:

$$\frac{\xi^{(TiN)}}{\xi^{(AlN)}} \approx \frac{1-x}{x} \quad , \tag{3.1.2}$$

$$\xi^{(TiN)} + \xi^{(AlN)} + \xi^{(m)} = 1 \quad , \tag{3.1.3}$$

$$\xi^{(TiN)} + \xi^{(AlN)} = \xi^{(p)} \quad . \tag{3.1.4}$$

Equation (3.1.2) states that the ratio of volume fractions of TiN and AlN is proportional to the ratio of the mole fractions of Ti and Al in the parent phase.

In table 3.1.1, the Young's moduli $E^{(\mathrm{p})}$, the Poisson numbers $\nu^{(\mathrm{p})}$ and the volume changes $\delta^{(\mathrm{p})}$ upon transformation of the $\mathrm{Ti}_{(1-x)}\mathrm{Al}_x\mathrm{N}$ matrix into TiN and AlN daughter phases are listed, evaluated by ab-initio modeling [23] for a number of different Al mole fractions (x). These are the values employed to define the material parameters in both analytical and numerical micromechanical methods, TFA and FEM.

x	$E^{(\mathrm{m})}$	$\nu^{(\mathrm{m})}$	$E^{(\mathrm{TiN})}$	$\nu^{(\mathrm{TiN})}$	$\delta^{(\mathrm{TiN})}$	$E^{(\mathrm{AlN})}$	$\nu^{(\mathrm{AlN})}$	$\delta^{(\mathrm{AlN})}$
[]	[GPa]	[]	[GPa]	[]	[]	[GPa]	[]	[]
0.0	414.0	0.25	414.0	0.25	0.0	378.0	0.25	−
0.25	400.50	0.25	414.0	0.25	+0.02396445	378.0	0.25	−0.10438249
0.50	387.00	0.25	414.0	0.25	+0.05195858	378.0	0.25	−0.07976260
0.66	381.00	0.25	414.0	0.25	+0.07472960	378.0	0.25	−0.06013910
0.75	378.01	0.25	414.0	0.25	+0.08965584	378.0	0.25	−0.04669945
1.0	378.0	0.25	414.0	0.25	−	378.0	0.25	0.0

Table 3.1.1: Material parameters of $\mathrm{Ti}_{(1-x)}\mathrm{Al}_x\mathrm{N}$ transforming into TiN and AlN evaluated by ab-initio modeling for a number of different Al mole fractions x [23].

Note that Young's moduli $E^{(\mathrm{p})}$ are quite similar (9% difference between TiN and AlN), Poisson numbers $\nu^{(\mathrm{p})}$ do not change and transformation strains $\delta^{(\mathrm{p})}$ in TiN and AlN have opposite signs. In the following, continuum micromechanical methods are used for estimating the transformation-induced SEDs of nano inhomogeneous phase arrangements of the type shown in figure 3.1.1 and 3.1.2.

3.2 Generation of Unit Cells

3.2.1 General Remarks

Three dimensional periodic cube-shaped unit cells with an edge length of e that contain a predefined number of monodisperse inclusions (spherical, cubic or tetrahedral shape) embedded in a matrix were meshed with Hypermesh. The inclusions are randomly distributed, of identical size and they do not overlap. The procedure followed in generating the underlying phase arrangement was the same as the one explained in [31, 34, 35], i.e., Random Sequential Insertion and Random Perturbation algorithms were employed. A relative scale is used to define length units for unit cell models throughout the present work.

The unit cell's size must be large enough to properly describe the composite behaviour and small enough in terms of computational requirements.

Four different sets of unit cell arrangements were generated and are defined by the following nomenclature:

- UCSP: unit cells containing spherical particles, and showing a matrix-inclusion topology

- UCCP: unit cells containing randomly oriented cube-shaped particles, and showing a matrix-inclusion topology

- UCTP: unit cells containing randomly oriented tetrahedral particles, and showing a matrix-inclusion topology

- UCRT: unit cells consisting of cube shaped regions each of which is randomly assigned to some phase such that the target phase volume fractions are reached. These voxel models constitute three-phase random composites (i.e., they do not necessarily show a matrix-inclusion topology).

Abaqus solid elements are used for the linear analysis. Second-order elements provide higher accuracy than first-order ones and they capture stress concentrations more efficiently. In combination with a tetrahedral element shape, they are able to model complex geometric features. Specifically, they can model phase arrangements with matrix-inclusion topology with fewer elements and more accurately compared to using linear elements, four-node tetrahedra being known to have suboptimal convergence properties [1].

Consequently, two types of volume element were employed:

- C3D10: second order continuum three-dimensional tetrahedral elements with 10 nodes and 4 integration points

- C3D20: second order continuum three-dimensional cubic elements with 20 nodes and 27 integration points

The meshes of unit cells UCSP, UCCP and UCTP are composed of C3D10 elements and UCRT uses C3D20 elements (the same element types are used for all phases in a given unit cell).

Another factor in modeling is element size. When unit cells formed by a small number of big elements are used, the results tend to be inaccurate, but the computational cost is reduced. A simple rule for choosing the cell size was taken: there should be at least two "layers" of elements in the matrix between any pair of neighbouring inhomogeneities. This way, stress fields between inclusions can be modeled sufficiently well.

As mentioned before, the unit cell must be periodic along the three directions X, Y and Z in both deformed and undeformed states. To fulfill this condition, periodicity boundary conditions are defined on the unit cell using the program MedTool 3.4 (a shell script manager developed at the ILSB by Pahr). Figures (3.2.1) and (3.2.2) show how periodicity holds for deformed and undeformed states of such unit cells.
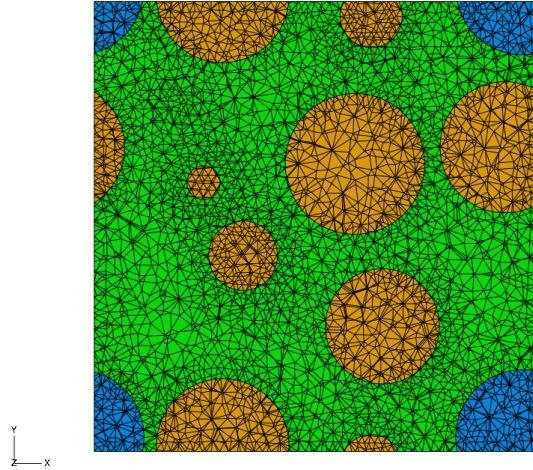
Figure 3.2.1: Undeformed random section in an XY-plane of unit cell arrangement UCSP for Al mole fraction $x = 0.50$. Green represents the $Ti_{0.5}Al_{0.5}N$ matrix, orange the TiN phase and blue the AlN phase. Particle volume fractions are $\xi^{(TiN)} = \xi^{(AlN)} = 0.2$.
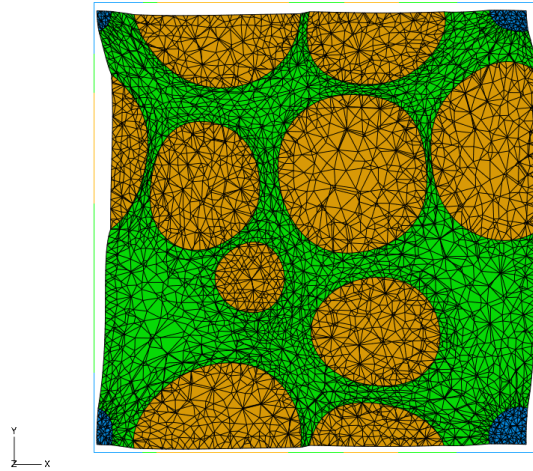

Figure 3.2.2: Deformed shape of the XY-section shown in 3.2.1 of unit cell arrangement UCSP after phase transformation for Al mole fraction $x = 0.50$ and unconstrained conditions. Green represents the $Ti_{0.5}Al_{0.5}N$ matrix, orange the TiN phase and blue the AlN phase. Particle volume fractions are $\xi^{(TiN)} = \xi^{(AlN)} = 0.2$. The deformation scale factor is 21.576.

For each set of phase arrangements five phase distributions were created by generating one unit cell geometry and then providing different random phase assignments for it. This was done by using a Python script employing a suitable random number generator. The purpose of this procedure is to estimate the dependence in the parameters of interest (strain energy density, overall thermal expansion tensor and stiffness matrix) and to remove fluctuations due to individual samples.

The underlying phase geometries contain some 20 and 24 particles, a number known to give reasonable approximations to elastic behaviour [7].

For unit cells UCSP, UCCP and UCTP, assignments of TiN and AlN to individual inhomogeneities was controlled by random selection within constraint of maintaining mole fraction; for UCRT phase assignment of each individual element (voxel) was under random control.

All cases studied are summarised in the following table (3.2.1):

Case	x	$\xi^{(p)}$	Mac. Constr.	UnitCell	Inclusions	Shape
[]	[]	[]	[]	[]	[]	[]
1	0.25	0.40	Unconstrained	UCSP	24	Spherical
2	0.50	0.40	Unconstrained	UCSP	24	Spherical
3	0.66	0.40	Unconstrained	UCSP	24	Spherical
4	0.75	0.40	Unconstrained	UCSP	24	Spherical
5	0.50	0.40	Fully Constrained	UCSP	24	Spherical
6	0.50	0.40	Layer Constraint	UCSP	24	Spherical
7	0.50	0.20	Unconstrained	UCCP	22	Cubic
8	0.50	0.20	Unconstrained	UCTP	20	Tetrahedral
9	0.50	0.50	Unconstrained	UCRT	–	–
10	0.50	0.66	Unconstrained	UCRT	–	–
11	0.50	0.90	Unconstrained	UCRT	–	–

Table 3.2.1: Set of phase arrangements studied for different combinations of Al mole fractions x, particle volume fractions $\xi^{(p)}$, macroscopic constraints and unit cell arrangements.

3.2.2 Matrix-Inclusion Topology

Matrix-inclusion topologies are characterized by having a special distribution of the constituents. The matrix phase is continuous, i.e., all inclusions are surrounded by matrix and it is possible to go through the unit cell from one face of the cell to the opposite one while staying within the contiguous matrix phase, see figure (3.2.3).
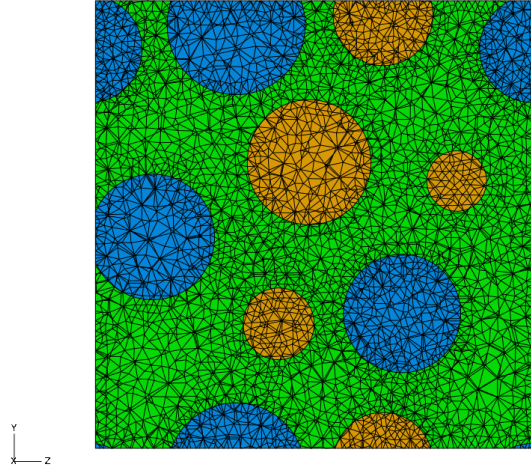
Figure 3.2.3: Undeformed random section in plane an XY-plane of unit cell arrangement UCSP for Al mole fraction $x = 0.50$. Green represents the $Ti_{0.5}Al_{0.5}N$ matrix, orange the TiN phase and blue the AlN phase. Particle volume fractions are $\xi^{(TiN)} = \xi^{(AlN)} = 0.2$.

Three shapes for the inclusions were considered: spheres, cubes and tetrahedra.

3.2.2.1 Spherical particles

The unit cell arrangement UCSP contains 24 spherical inclusions ($r = 0.15846e$, where r is the radius of the inclusions) of TiN and AlN embedded in a $Ti_{(1-x)}Al_xN$ matrix. This number of particles can be estimated to be sufficient for providing reliable results [35]. Also, there is a physical limit in terms of the maximum particle volume fraction that can be reached, $\xi^{(p)}_{max,phys} = 0.74$. This limit arises because the fcc and hcp packings are the densest ones that can be reached with spheres of equal size.

Within the present work periodic arrangements of spheres are generated by program PARGEN, an in-house code based on the work of Segurado [34]. It combines Random Sequential Insertion and Random Perturbation algorithms to reach maximum particle volume fractions of about $\xi^{(p)}_{max,alg} = 0.50$. To ensure that particle arrangements can be meshed without undue difficulty, a minimum particle distance of $d^{(int-p)}_{min} = 0.025e$ and a minimum distance of the spheres' surfaces from the cell faces of $d^{(cell-bounds)}_{min} = 0.025e$ were selected.

Figure 3.2.4 shows the UCSP mesh for the particular case of Al mole fraction $x = 0.5$ and in figures 3.2.5 to 3.2.9 and 3.2.10 TiN (orange color) and AlN (blue color) spherical particles and $Ti_{0.5}Al_{0.5}N$ matrix (green color) can be easily distinguished.

Also, in figures 3.2.5 to 3.2.9 the five sets of particle assignments of a unit cell of the type UCSP ($x = 0.50$ and $\xi^{(m)} = 0.6$) are displayed.
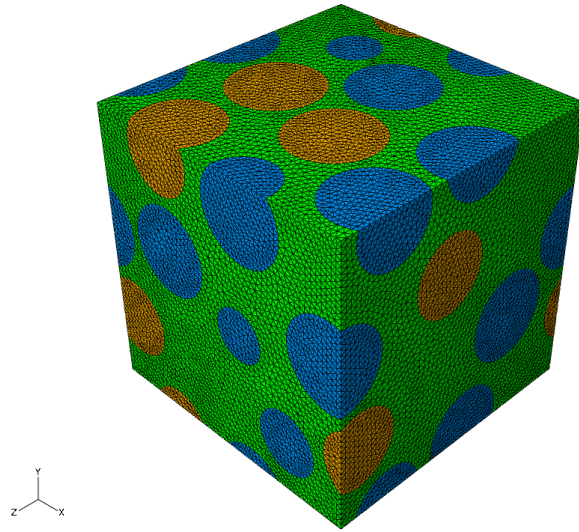
Figure 3.2.4: Unit cell arrangement UCSP containing 24 spherical inclusions (total particle volume fraction $\xi^{(\mathrm{p})} = 0.4$) for Al mole fraction $x = 0.50$. Green represents the $\mathrm{Ti}_{0.5}\mathrm{Al}_{0.5}\mathrm{N}$ matrix, orange the TiN phase and blue the AlN phase.
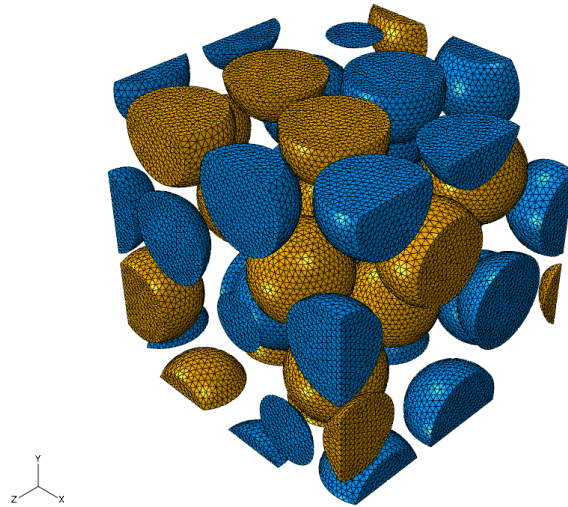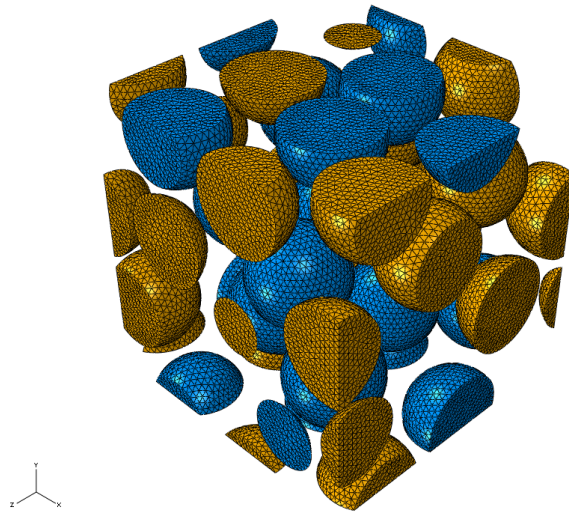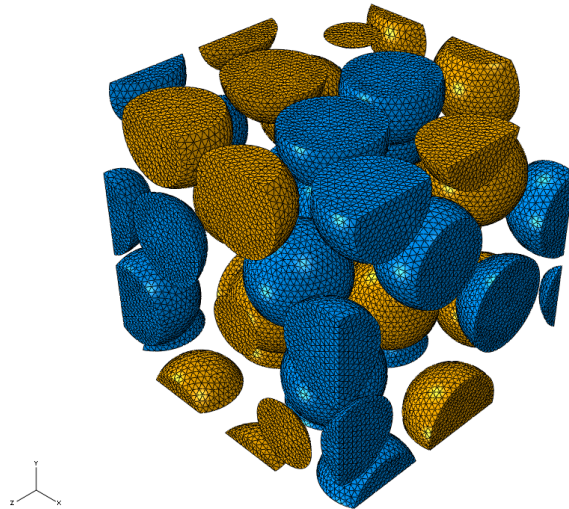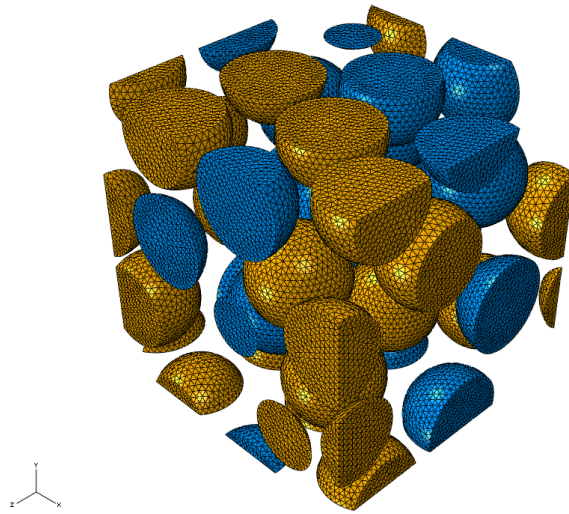

Figure 3.2.5: TiN and AlN spherical particles (volume fractions $\xi^{(\mathrm{TiN})} = \xi^{(\mathrm{AlN})} = 0.2$) contained in unit cell arrangement UCSP for Al mole fraction $x = 0.50$ for phase assignment #1. Orange represents the TiN phase and blue the AlN phase.
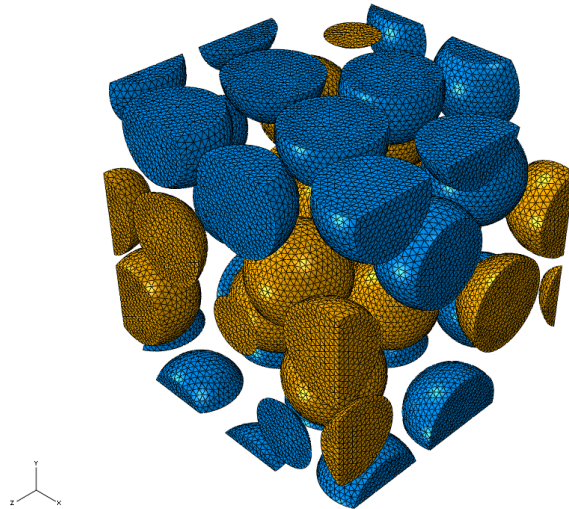
Figure 3.2.6: TiN and AlN spherical particles (volume fractions $\xi^{(\mathrm{TiN})} = \xi^{(\mathrm{AlN})} = 0.2$) contained in unit cell arrangement UCSP for Al mole fraction $x = 0.50$ for phase assignment #2. Orange represents the TiN phase and blue the AlN phase.


Figure 3.2.7: TiN and AlN spherical particles (volume fractions $\xi^{(\mathrm{TiN})} = \xi^{(\mathrm{AlN})} = 0.2$) contained in unit cell arrangement UCSP for Al mole fraction $x = 0.50$ for phase assignment #3. Orange represents the TiN phase and blue the AlN phase.

Figure 3.2.8: TiN and AlN spherical particles (volume fractions $\xi^{(\mathrm{TiN})} = \xi^{(\mathrm{AlN})} = 0.2$) contained in unit cell arrangement UCSP for Al mole fraction $x = 0.50$ for phase assignment #4. Orange represents the TiN phase and blue the AlN phase.

Figure 3.2.9: TiN and AlN spherical particles (volume fractions $\xi^{(\mathrm{TiN})} = \xi^{(\mathrm{AlN})} = 0.2$) contained in unit cell arrangement UCSP for Al mole fraction $x = 0.50$ for phase assignment #5. Orange represents the TiN phase and blue the AlN phase.
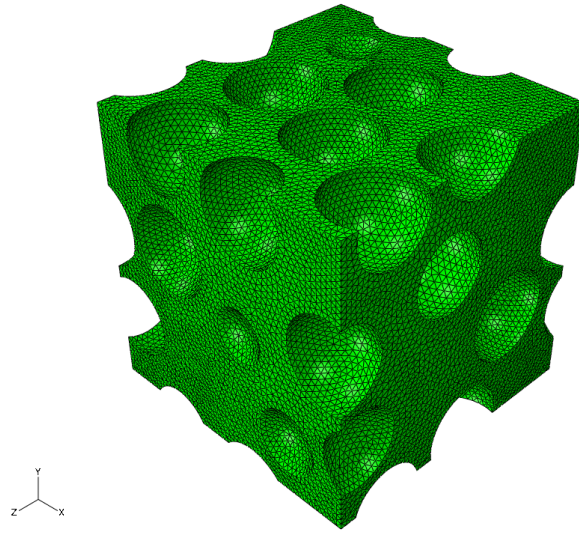
Figure 3.2.10: $Ti_{0.5}Al_{0.5}N$ matrix (volume fraction $\xi^{(m)} = 0.6$) contained in the unit cell arrangement UCSP.

3.2.2.2 Cube-shaped particles

The unit cell arrangement UCCP contains 22 cube-shaped inclusions ($l = 0.2087e$, where l is the edge length of the inclusions) of TiN and AlN embedded in a $Ti_{0.5}Al_{0.5}N$ matrix with a particle volume fraction of $\xi^{(p)} = 0.20$. This unit cell is one of a number of phase arrangements developed by Rasool [31].

Figure 3.2.11 shows the UCCP mesh and in figure 3.2.12 TiN (orange color) and AlN (blue color) cube-shaped particles are displayed for one of the five phase assignments.
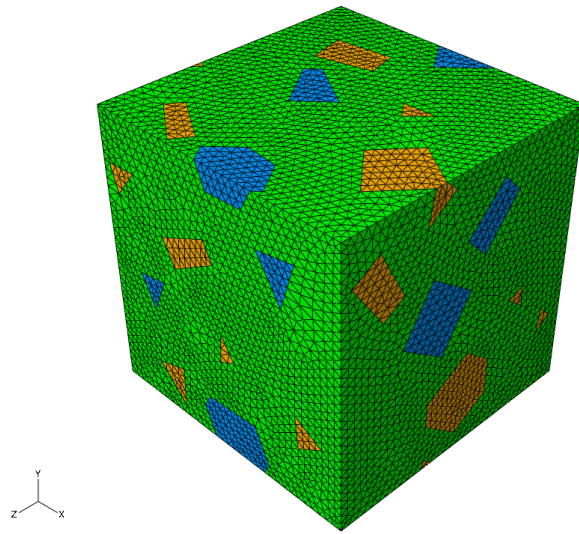
Figure 3.2.11: Unit cell arrangement UCCP containing 22 cube-shaped inclusions (volume fraction $\xi^{(\mathrm{p})} = 0.2$) for Al mole fraction $x = 0.50$. Green represents the $\mathrm{Ti}_{0.5}\mathrm{Al}_{0.5}\mathrm{N}$ matrix, orange the TiN phase and blue the AlN phase.
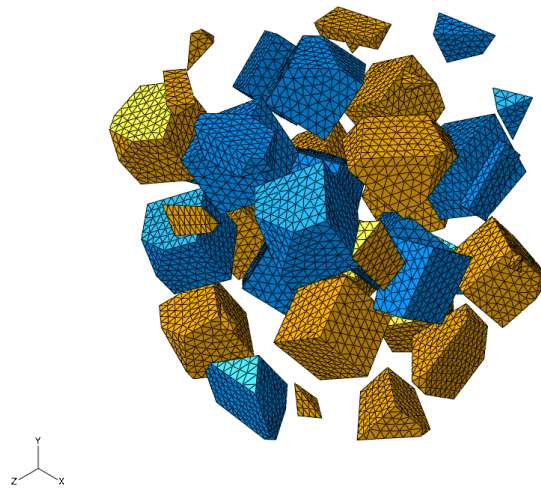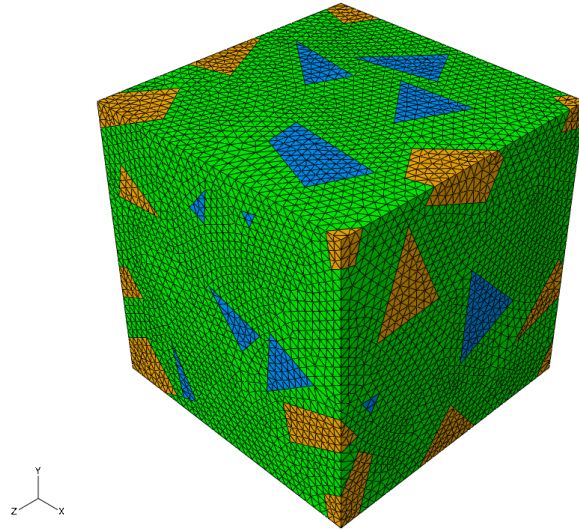

Figure 3.2.12: TiN and AlN cube-shaped particles (volume fractions $\xi^{(\mathrm{TiN})} = \xi^{(\mathrm{AlN})} = 0.1$) contained in unit cell arrangement UCCP for Al mole fraction $x = 0.50$. Orange represents the TiN phase and blue the AlN phase.

3.2.2.3 Tetrahedral particles

The unit cell arrangement UCTP contains 20 tetrahedral inclusions ($l = 0.4394e$, where l is the edge length of the inclusions) of TiN and AlN embedded in a $Ti_{0.5}Al_{0.5}N$ matrix. The particle volume fraction is $\xi^{(p)} = 0.20$. This unit cell was also taken from the doctoral thesis of Rasool [31].

Figure 3.2.13 shows the UCSP mesh and in figure 3.2.14 TiN (orange color) and AlN (blue color) tetrahedral particles are displayed for one of the five phase assignments.

Figure 3.2.13: Unit cell arrangement UCTP containing 20 tetrahedral inclusions (volume fraction $\xi^{(p)} = 0.2$) for Al mole fraction $x = 0.50$. Green represents the $Ti_{0.5}Al_{0.5}N$ matrix, orange the TiN phase and blue the AlN phase.
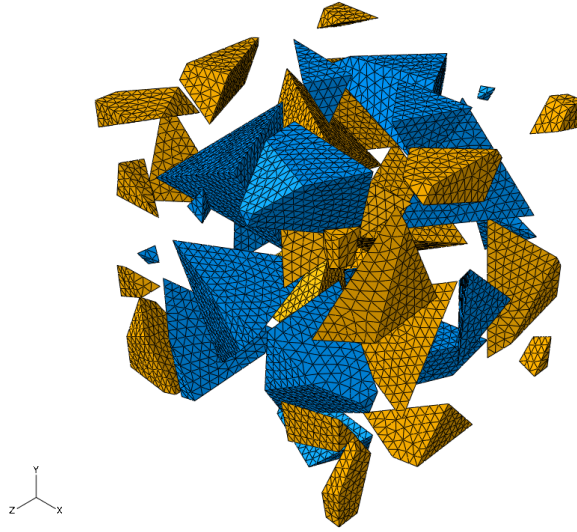
Figure 3.2.14: TiN and AlN tetrahedral particles (volume fractions $\xi^{(\text{TiN})} = \xi^{(\text{AlN})} = 0.1$) contained in unit cell arrangement UCTP for Al mole fraction $x = 0.50$. Orange represents the TiN phase and blue the AlN phase.

3.2.3 Random Topology

As mentioned in chapter 3.1 the real topology of $\text{Ti}_{(1-x)}\text{Al}_x\text{N}$ appears to be an interpenetrating one. The phase assignments of individual voxels in data such as those depicted in figures 3.1.1 and 3.1.2 could not be assessed for technical reasons, so that the elastic strain energies of these phase arrangements could not be evaluated. In order to asses the strain energy densities of phase arrangements that do not show straightforward matrix-inclusion topology, random three-phase geometries were studied.

The unit cell arrangement UCRT consists of a regular array of 50x50x50 = 125000 cube-shaped elements (voxels of edge length $l = 0.02e$), randomly assigned to the TiN, AlN or $\text{Ti}_{0.5}\text{Al}_{0.5}\text{N}$ phases to attain the required phase volume fractions, see figure 3.2.15.

The accuracy of the microfields evaluated from arrangement UCRT can be expected to be lower than those obtained from cells UCSP, UCCP and UCTP. In volume element UCRT, the smallest possible phase region is a single element of 20 nodes (and thus 60 displacement degrees of freedom). In addition, in arrangements UCSP, UCCP and UCTP all inclusions are convex, whereas in UCRT any phase must be expected to have non-convex regions. Together with the voxel-type meshing scheme, compare figure 2.4.1, this leads to re-entrant corners that may give rise to artificial stress concentrations in the FE approximations and to singularities in the exact elasticity solution. Such issues with pixel and voxel type meshes are well known and were discussed , e.g., by [12, 27, 32, 37].

Figures 3.2.15 and 3.2.16 show one of the microgeometries generated for $\xi^{(\text{TiAlN})} = 0.5$, $\xi^{(\text{TiN})} = \xi^{(\text{AlN})} = 0.25$. Here only the parent phase is contiguous and the microtopology can be classified as being of the matrix-inclusion type. In contrast to the phase

arrangements discussed in section 3.2.2, however, the two daughter phases may contact directly (i.e., without intervening matrix as, e.g., in figure 3.2.3) and their domains may be non-convex.

For phase volume fractions of $\xi^{(\text{TiAlN})} = 0.34$, $\xi^{(\text{TiN})} = \xi^{(\text{AlN})} = 0.33$, a different picture emerges. Here, all three phases are on an equal footing topologically, and none of them is clearly contiguous, compare figures 3.2.17 and 3.2.18. This microstructure is more closely related to grain-type ones, i.e., it may be viewed as a special type of a polycrystal.

Finally, for $\xi^{(\text{TiAlN})} = 0.1$, $\xi^{(\text{TiN})} = \xi^{(\text{AlN})} = 0.45$, there are inclusions of the parent phase embedded in a region of interpenetrating daughter phases, compare figures 3.2.19 and 3.2.20.

Evidently, three-phase random voxel-type microstructures can lead to a range of microtopologies, depending on the phase volume fractions.
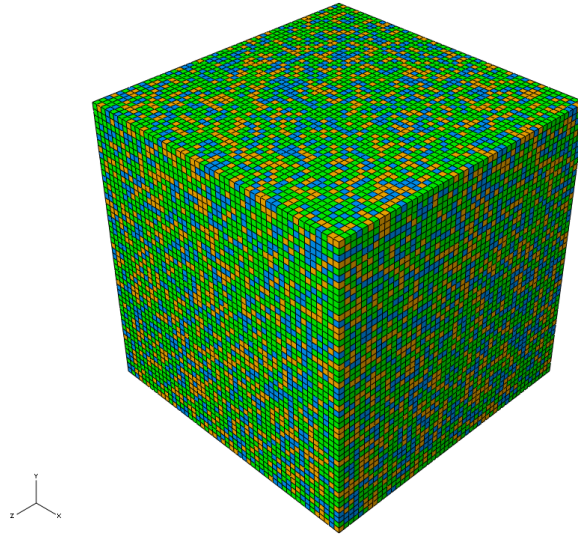

Figure 3.2.15: Unit cell arrangement UCSP for Al mole fraction $x = 0.50$ (phase volume fractions $\xi^{(\text{TiAlN})} = 0.5$, $\xi^{(\text{TiN})} = 0.25$ and $\xi^{(\text{AlN})} = 0.25$) consisting of 125000 cube-shaped elements. Green represents $\text{Ti}_{0.5}\text{Al}_{0.5}\text{N}$, orange TiN and blue AlN.
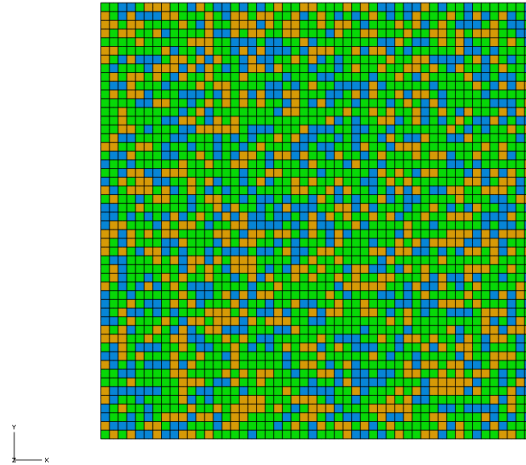
Figure 3.2.16: Random section in an XY-plane of unit cell arrangement UCRT for Al mole fraction $x = 0.50$ (phase volume fractions $\xi^{(\text{TiAlN})} = 0.5$, $\xi^{(\text{TiN})} = 0.25$ and $\xi^{(\text{AlN})} = 0.25$). Green represents $\text{Ti}_{0.5}\text{Al}_{0.5}\text{N}$, orange TiN and blue AlN.
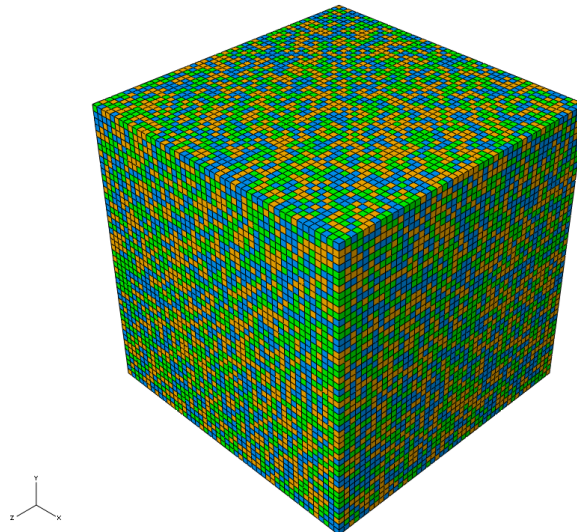

Figure 3.2.17: Unit cell arrangement UCSP for Al mole fraction $x = 0.50$ (phase volume fractions $\xi^{(\text{TiAlN})} = 0.34$, $\xi^{(\text{TiN})} = 0.33$ and $\xi^{(\text{AlN})} = 0.33$) consisting of 125000 cube-shaped elements. Green represents $\text{Ti}_{0.5}\text{Al}_{0.5}\text{N}$, orange TiN and blue AlN.
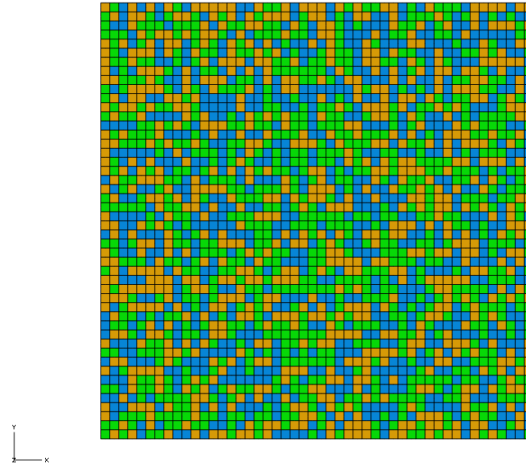
Figure 3.2.18: Random section in an XY-plane of unit cell arrangement UCRT for Al mole fraction $x = 0.50$ (phase volume fractions $\xi^{(\text{TiAlN})} = 0.34$, $\xi^{(\text{TiN})} = 0.33$ and $\xi^{(\text{AlN})} = 0.33$). Green represents $\text{Ti}_{0.5}\text{Al}_{0.5}\text{N}$, orange TiN and blue AlN.
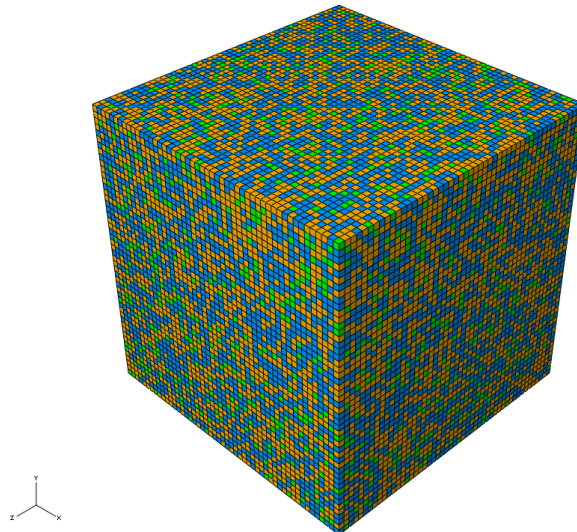

Figure 3.2.19: Unit cell arrangement UCSP for Al mole fraction $x = 0.50$ (phase volume fractions $\xi^{(\text{TiAlN})} = 0.1$, $\xi^{(\text{TiN})} = 0.45$ and $\xi^{(\text{AlN})} = 0.45$) consisting of 125000 cube-shaped elements. Green represents $\text{Ti}_{0.5}\text{Al}_{0.5}\text{N}$, orange TiN and blue AlN.
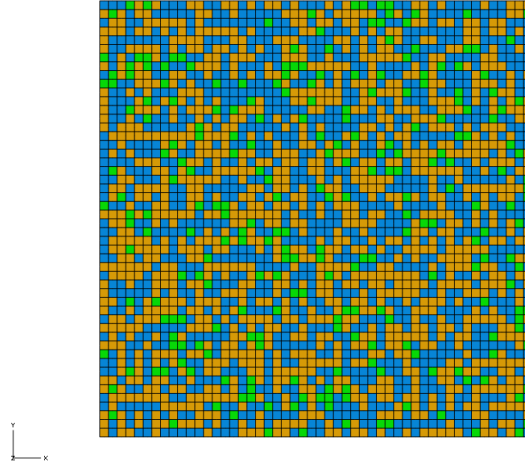
Figure 3.2.20: Random section in an XY-plane of unit cell arrangement UCRT for Al mole fraction $x = 0.50$ (phase volume fractions $\xi^{(\text{TiAlN})} = 0.1$, $\xi^{(\text{TiN})} = 0.45$ and $\xi^{(\text{AlN})} = 0.45$). Green represents $\text{Ti}_{0.5}\text{Al}_{0.5}\text{N}$, orange TiN and blue AlN.

3.3 Boundary Conditions and Constraints

Periodicity boundary conditions are applied to the unit cells in order to link microscopic and macroscopic states. They restrain the relative displacements between opposite faces, so that these fit into each other in both undeformed and deformed states. Further explanations can be found in chapter 2.5.2.

To simplify understanding, the following nomenclature is used for the faces of the unit cells: East (E), West (W), North (N), South (S), Top (T), Bottom (B), compare figure 2.5.4. Accordingly, edges and vertices are defined by the intersection of faces, so that SWB, NWB, SWT, NWT, SEB, NEB, SET, NET (see figure 3.3.1) are unique designators for the vertices.

3.3.1 Macroscopic Constraints

Three sets of macroscopic constraints are applied via the three master nodes (NWB, SWT, SEB) that control the deformation of the unit cell arrangements: unconstrained, fully constrained and layer constraint case. Node SWB is completely fixed, i.e., it cannot translate in any direction.

3.3.1.1 Unconstrained Case

In this case, node NWB is restrained in X, SWT in Y, SEB in Z-direction and node SWB is anchored. These constraints represent an infinite periodic material that can deform freely in all directions. Under these conditions the transformations in general lead to nonzero macroscopic strains, whereas the macroscopic stresses must vanish.
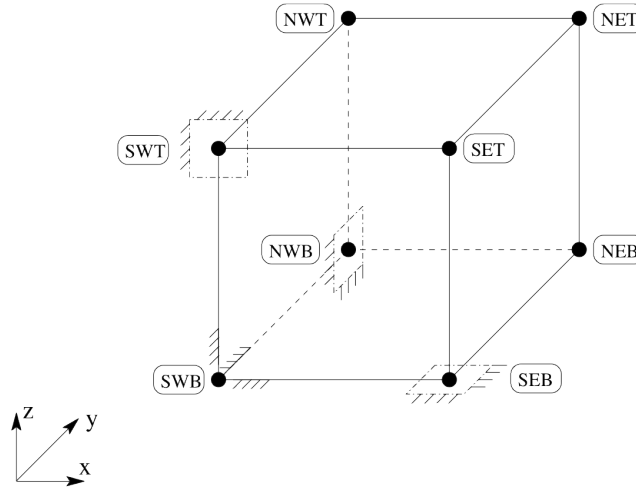

Figure 3.3.1: Schematic representation of a unit cell for the unconstrained case.

3.3.1.2 Fully Constrained Case

In this case, all master nodes, NWB, SWT, SEB and SWB are anchored. These constraints represent an infinite periodic material that is not allowed to deform macroscopically (periodic microscopic deformations are allowed, however). Under these conditions there are zero macroscopic strains upon transformation, whereas the macroscopic stresses in general are nonzero.
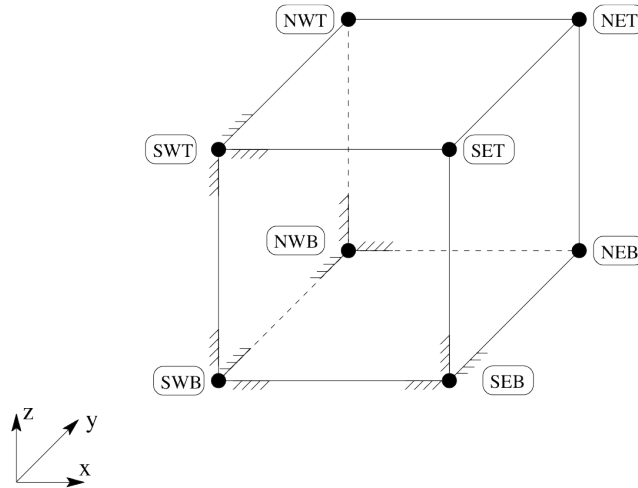
Figure 3.3.2: Schematic representation of a unit cell for the fully constrained case.

3.3.1.3 Layer Constraint Case

In this case, nodes NWB, SWT and SWB are anchored and node SEB is restrained in Y and Z-direction. These conditions describe a coating, a thin layer deposited on a stiff substrate, that only can be deformed in the normal direction X to its plane of residence YZ. Under these conditions in general neither the macroscopic stress nor the macroscopic strain tensors are zero upon transformation.
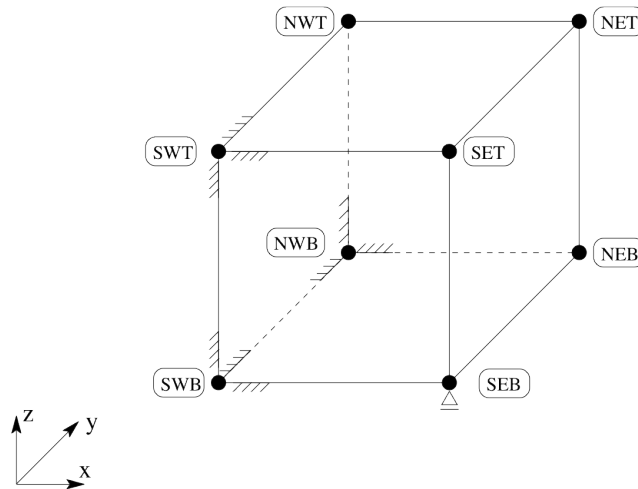

Figure 3.3.3: Schematic representation of a unit cell for the layer constraint case.

3.4 Load Cases

Seven load cases are applied to the unit cells in the present study.

- The thermoelastic capabilities of the program are employed for modeling the phase transformation and the volume changes $\delta^{(\mathrm{p})}$ listed in table 3.1.1 are applied via thermal expansions. This is done by setting the coefficients of thermal expansion of the phases to $\alpha^{(\mathrm{p})} = \delta^{(\mathrm{p})}/3$ and applying a temperature increase of $\Delta\mathrm{T} = 1\mathrm{K}$. This way, the SED is obtained and the macroscopic transformation strain $\mathbf{e}^*$ can be evaluated from the deformations of the master nodes (the macroscopic stress contribution $\mathbf{s}^*$ is obtained in analogy from the reaction forces of the master nodes).

- Six linearly independent mechanical loading cases (three tensile loads and three shear loads) allow to compute the effective elasticity matrix. This information is not the main goal in the present work, but it helps in assessing the deviations of the phase arrangements from macroscopic isotropy.

4 Results and Discussion

In this chapter results obtained for the different unit cells are analyzed, interpreted and explained. The principal study is done on the SED and on its dependence on phase geometry and phase properties. Meshes of the unit cells were analyzed to check the real volume fraction of the phases (IVOL). A Zener factor (A) was also calculated in order to asses the deviation from isotropic macroscopic behaviour of the composite RVEs.

4.1 General Remarks

4.1.1 Computer analysis

In order to check if the particle volume fractions of the unit cell meshes generated with Hypermesh match with the targeted value, the volumes of the integration points (IVOL) are evaluated. Once all the IVOL values of each phase were added, the results showed that the maximum difference between the real and target volume fractions was about $0.025\,\%$, small enough to guarantee the reliability of the unit cell meshes.

To perform the finite element analyses, Abaqus V.6.9-1 [1] was used. Linear analyses were carried out because the strain along the three main directions (X, Y, Z) is less than one per cent ($\varepsilon_X \approx \varepsilon_Y \approx \varepsilon_Z \leq 1\,\%$). No large-displacement formulation was used for the step calculation.

The SED results obtained with Abaqus in the five samples of each of the eleven cases (table 3.2.1) are extremely similar. Consequently, the standard deviation of these samples can be approximated as zero, and no error bars are displayed in the graphics where SED is plotted. In the following, $\overline{w_\mathrm{e}}$ will denote the SED mean value of the 5 samples.

Analytical results based on the Transformation Field Analysis and Mori-Tanaka methods are computed with TRFMULT, it is an in-house program developed at the ILSB by Böhm, which allows to evaluate the strain energies of inhomogeneous materials with different micromechanical models.

4.1.2 Material Properties

Previous investigations [23] have demonstrated that $\left|(1-x)\delta^{(\mathrm{TiN})}\right| \leq \left|x\delta^{(\mathrm{AlN})}\right|$ (see figure 4.1.1), so that the volume change associated with the formation of TiN and AlN particles is negative for any Al mole fraction. Figure 4.1.2 shows the macroscopic shrinkage of a unit cell of the type UCSP (one of five sets of particle assignments for $x = 0.50$ and $\xi^{(\mathrm{m})} = 0.6$) after transformation.
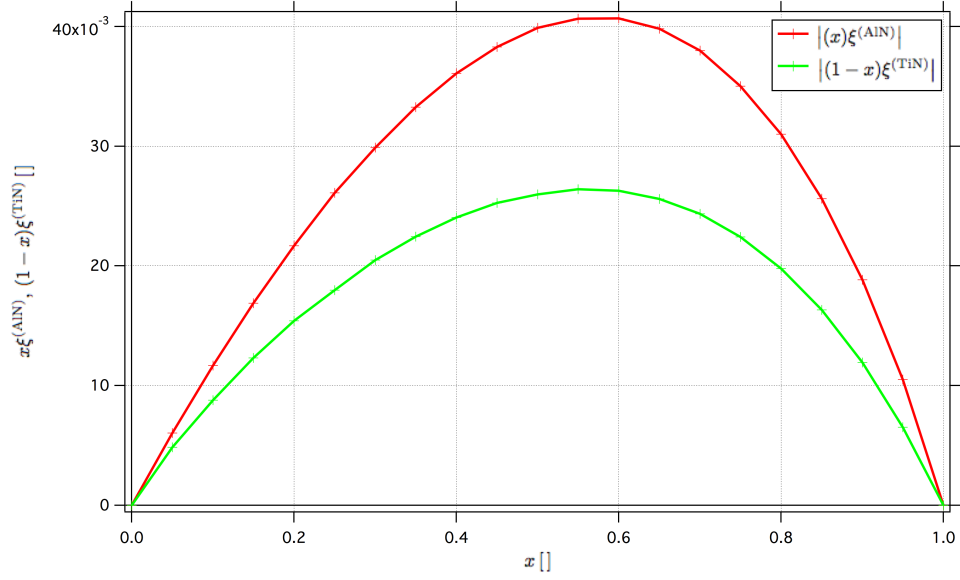
Figure 4.1.1: Absolute value of phase mole fraction times phase volume change $((1-x)\delta^{(\mathrm{TiN})}$ and $x\delta^{(\mathrm{AlN})})$ for the decomposition of $\mathrm{Ti}_{(1-x)}\mathrm{Al}_x\mathrm{N}$ to form TiN and AlN, respectively.

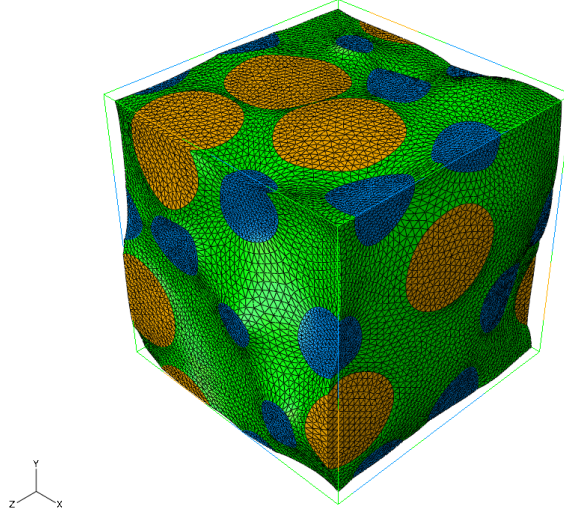Figure 4.1.2: Deformed shape of one unit cell of type UCSP after transformation, for an Al mole fraction $x = 0.50$, phase volume fractions $\xi^{(\mathrm{TiAlN})} = 0.6$, $\xi^{(\mathrm{TiN})} = 0.2$ and $\xi^{(\mathrm{AlN})} = 0.2$ and unconstrained conditions. Green represents the $\mathrm{Ti}_{0.5}\mathrm{Al}_{0.5}\mathrm{N}$ matrix, orange the TiN phase and blue the AlN phase. The deformation scale factor is 21.576.

As expected from the phase material parameters (see table 3.1.1), the TiN particles grow due to a positive $\delta^{(\text{TiN})}$, the AlN particles shrink due to a negative $\delta^{(\text{AlN})}$ and the $\text{Ti}_{(1-x)}\text{Al}_x\text{N}$ matrix adapts to the particles' deformation due to $\delta^{(\text{m})} = 0$. This behaviour can be seen in figures 4.1.3, 4.1.4 and 4.1.5.
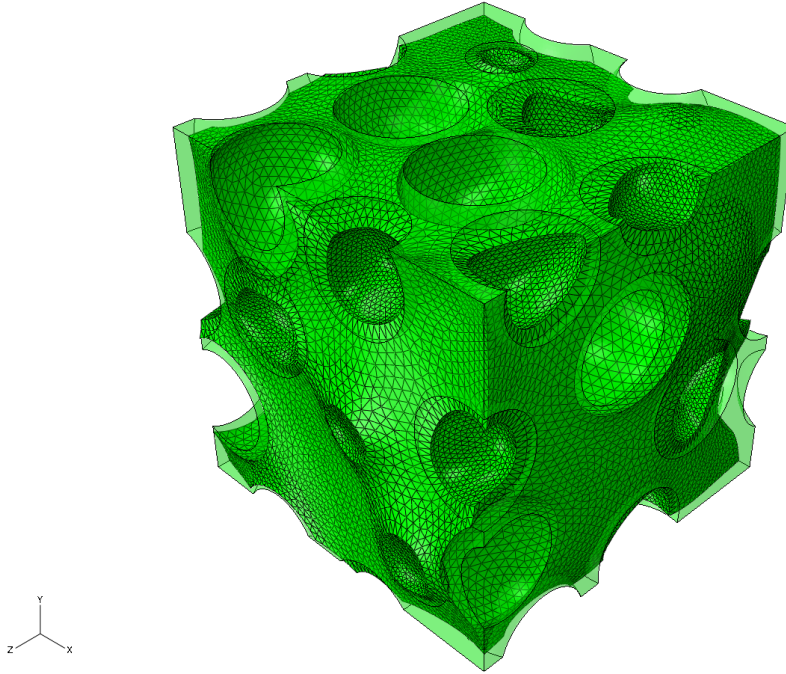

Figure 4.1.3: Deformed (solid mesh) and undeformed (shaded solid) $\text{Ti}_{0.5}\text{Al}_{0.5}\text{N}$ matrix after transformation, as obtained for one unit cell of type UCSP for matrix volume fraction $\xi^{(\text{TiAlN})} = 0.6$ and unconstrained conditions. The deformation scale factor is 21.576.

Figure 4.1.4: Deformed (solid mesh) and undeformed (shaded solid) TiN particles after transformation, as obtained for one unit cell of type UCSP for an Al mole fraction $x = 0.50$, $\xi^{(\mathrm{TiN})} = 0.2$ and unconstrained conditions. The deformation scale factor is 21.576.
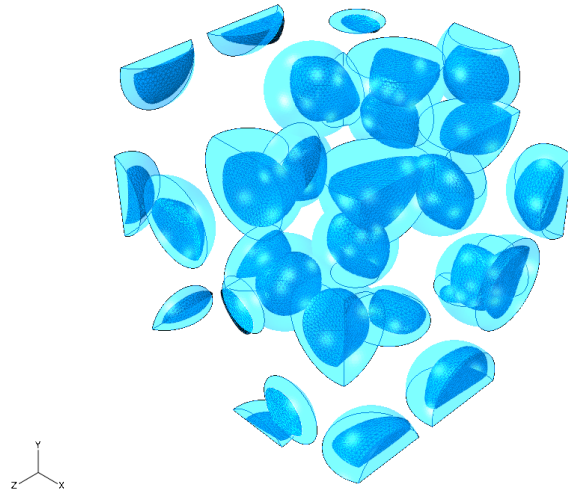

Figure 4.1.5: Deformed (solid mesh) and undeformed (shaded solid) AlN particles after transformation, as obtained for one unit cell of type UCSP for an Al mole fraction $x = 0.50$, $\xi^{(\mathrm{AlN})} = 0.2$ and unconstrained conditions. The deformation scale factor is 21.576.

The elastic symmetry of the composite was also evaluated. The macroscopic engineer-

ing constants E_1, E_2 and E_3 were calculated for each case and compared, computing the standard deviation of the three values. A low dispersion of the averages of E_1, E_2 and E_3 indicated isotropic or, possibly, cubic symmetry. In order to clarify the material symmetry, the Zener factor, A, was calculated via equation (4.1.1).

$$A = \frac{2E_{44}}{E_{11} - E_{12}} \tag{4.1.1}$$

It represents the deviation from isotropic macroscopic elastic symmetry of the composite RVE; the material has an isotropic symmetry if the value of A is unity. The results for the Zener factor shown in table (4.1.1) indicate that the elastic symmetry of both random and matrix-inclusion topologies is isotropic.

Case	x	$\xi^{(p)}$	Mac. Constr.	UnitCell	E_{11}	E_{12}	E_{44}	A
[]	[]	[]	[]	[]	[GPa]	[GPa]	[GPa]	[]
1	0.25	0.40	Unconstrained	UCSP	482.621	160.852	160.865	0.999
2	0.50	0.40	Unconstrained	UCSP	468.517	156.138	156.154	0.999
3	0.66	0.40	Unconstrained	UCSP	461.314	153.757	153.772	0.999
4	0.75	0.40	Unconstrained	UCSP	457.766	152.563	152.576	0.999
9	0.50	0.50	Unconstrained	UCRT	471.292	157.071	157.101	0.999
10	0.50	0.66	Unconstrained	UCRT	469.561	156.500	156.522	0.999
11	0.50	0.90	Unconstrained	UCRT	473.727	157.875	157.913	0.999

Table 4.1.1: List of results for the Zener factor, A, calculated for different combinations of Al mole fractions (x), daughter phase volume fraction ($\xi^{(p)}$) and unit cell arrangements. Values for E_{11}, E_{12}, E_{44} are averages from five different assignments of daughter phases to the particles.

4.2 Strain Energy Density

Abaqus computes local (w_e) and average values ($\widetilde{w}_e$) of the strain energy density. Local values are defined for each integration point of the mesh and the average value is defined with respect to the total volume of the unit cell.

In this work, only the the average values are taken into account, even though local values may provide useful information on the behaviour of the phases upon transformation. As can be seen in figures 4.2.1, 4.2.2 and 4.2.3 local values of the SED are not uniform in the three phases of the composite. Also, the phase averages of the SED for $Ti_{0.5}Al_{0.5}N$, TiN and AlN differ, with values of 51 $[MJ/m^3]$, 18.3 $[MJ/m^3]$ and 32.6 $[MJ/m^3]$, respectively, being obtained. Studying equations (2.6.2) and (2.6.3) can explain both facts: on the one hand, w_e depends on the stress-strain state of each integration point and on the other hand, w_e depends on $\xi^{(i)}$ and $\mathbf{e}^{(i)}$ of the inclusions.
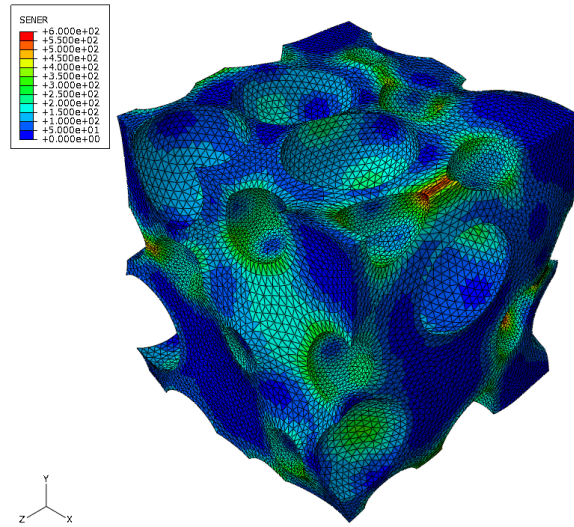
Figure 4.2.1: Predicted distribution of the strain energy w_e in the $Ti_{0.5}Al_{0.5}N$ matrix after transformation evaluated for one unit cell of type UCSP, phase volume fractions $\xi^{(TiAlN)} = 0.6$, $\xi^{(TiN)} = 0.2$ and $\xi^{(AlN)} = 0.2$ and unconstrained conditions. The deformation scale factor is 21.576.

Figure 4.2.2: Predicted distribution of the strain energy w_e in the TiN particles after transformation evaluated for one unit cell of type UCSP, Al mole fraction $x = 0.50$, phase volume fraction $\xi^{(TiN)} = 0.2$ and unconstrained conditions. The deformation scale factor is 21.576.
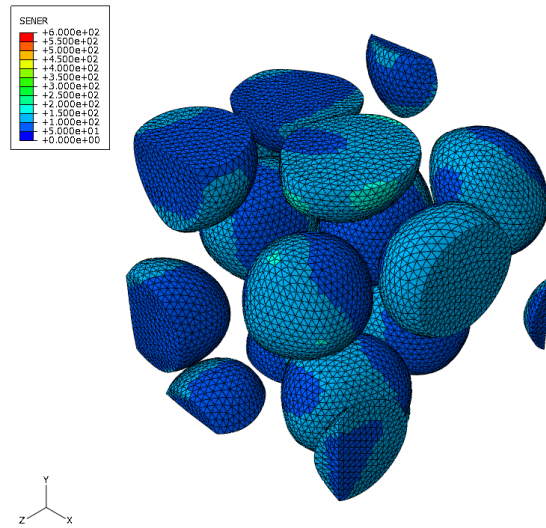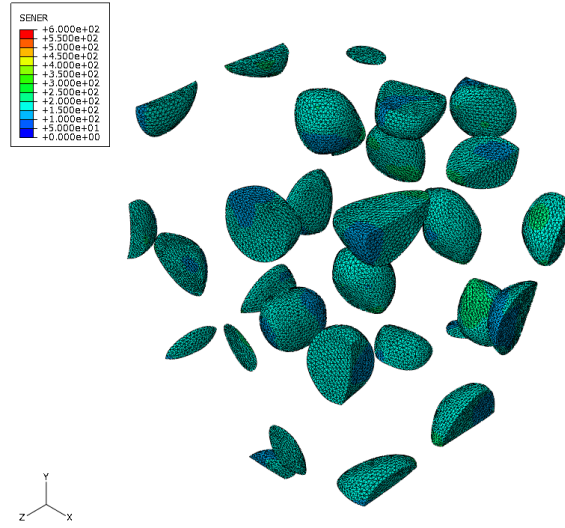
Figure 4.2.3: Predicted distribution of the strain energy w_e in the AlN particles after transformation evaluated for one unit cell of type UCSP, Al mole fraction $x = 0.50$, phase volume fraction $\xi^{(\mathrm{AlN})} = 0.2$ and unconstrained conditions. The deformation scale factor is 21.576.

4.2.1 Influence of the Al Mole Fraction x on SED

The strain energy density $(\overline{w_e})$ results of cases 1 to 4, where the Al mole fraction x takes the values of 0.25, 0.50, 0.66 and 0.75, are displayed in table 4.2.1. From figure (4.2.4) it is clear that the Al mole fraction x and $\overline{w_e}$ do not follow a linear relationship; this relationship can be approximated with a second order polynomial function:

$$\overline{w_e} = -416.20x^2 + 416.20x \qquad , 0 \leq x \leq 1 \qquad . \tag{4.2.1}$$

Note that this approximation is only valid for arrangement UCSP and a particle volume fraction $\xi^{(\mathrm{p})} = 0.4$, reaching a maximum of $\overline{w}_{\mathrm{e,max}}^{\mathrm{unconstr}} = 104.05\,\mathrm{MJ/m^3}$ for $x \approx 0.50$.

TFA results given in [5], compare also figure 4.3.1, consistently show that the SED is a linear function of the matrix volume fraction $\xi^{(\mathrm{m})}$ (and thus also of the total particle volume fraction $\xi^{(\mathrm{p})}$) for given microtopology, constraint conditions and Al mole fraction. On this basis, the above unit cell results for arrangement UCSP at $\xi^{(\mathrm{p})} = 0.4$ can be used to evaluate linear relationships of $\overline{w_e}(\xi^{(\mathrm{p})})$ as listed in table 4.2.1.

Case	x	$\xi^{(\mathrm{p})}$	Mac. Constr.	UnitCell	$\overline{w_{\mathrm{e}}}$	Equation
[]	[]	[]	[]	[]	$\left[\mathrm{MJ/m^3}\right]$	[]
1	0.25	0.40	Unconstrained	UCSP	72.93	$\overline{w_{\mathrm{e}}} = 182.34\xi^{(\mathrm{p})}$
2	0.50	0.40	Unconstrained	UCSP	102.76	$\overline{w_{\mathrm{e}}} = 256.90\xi^{(\mathrm{p})}$
3	0.66	0.40	Unconstrained	UCSP	96.19	$\overline{w_{\mathrm{e}}} = 240.47\xi^{(\mathrm{p})}$
4	0.75	0.40	Unconstrained	UCSP	82.38	$\overline{w_{\mathrm{e}}} = 205.95\xi^{(\mathrm{p})}$

Table 4.2.1: List of results of $\overline{w_{\mathrm{e}}}$ computed with unit cell arrangement UCSP, for different Al mole fractions (x), at a particle volume fraction $\xi^{(\mathrm{p})} = 0.4$ and unconstrained conditions. Values for $\overline{w_{\mathrm{e}}}$ are averages from five different assignments of daughter phases to the particles.
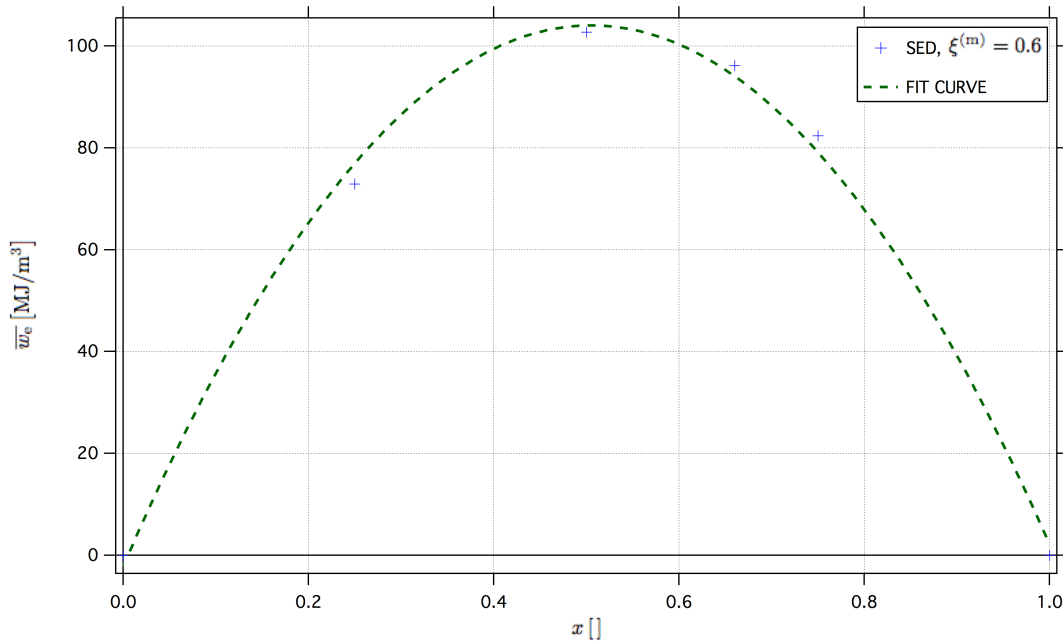

Figure 4.2.4: Strain energy density, calculated by FEM-based unit cells, as function of the Al mole fractions x in the three-phase system consisting of spherical TiN and AlN particles in a $\mathrm{Ti}_{(1-x)}\mathrm{Al}_x\mathrm{N}$ matrix for a matrix volume fraction $\xi^{(\mathrm{m})} = 0.6$ and unconstrained conditions.

These linear relationships between $\xi^{(\mathrm{m})}$ and $\overline{w_{\mathrm{e}}}$ are plotted in figure 4.2.5 for different values of the Al mole fractions x. As explained in chapter 3.2.2.1, there is a physical limit $\xi^{(\mathrm{p})}_{\mathrm{max,phys}} = 0.74$ (equivalent to $\xi^{(\mathrm{m})}_{\mathrm{min,phys}} = 0.26$ due to $\xi^{(\mathrm{p})} + \xi^{(\mathrm{m})} = 1$) for packings of spherical particles of equal size. Accordingly, for $\xi^{(\mathrm{m})} < 0.26$ $\overline{w_{\mathrm{e}}}$ cannot be evaluated
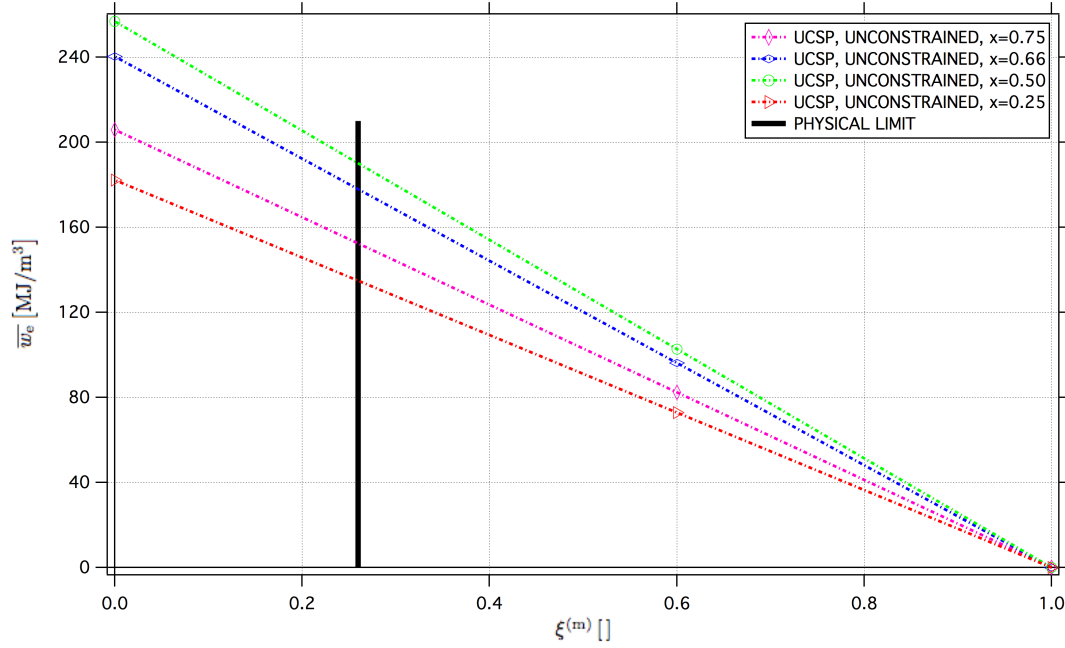
with volume elements of the UCSP type.

Figure 4.2.5: Strain energy density, calculated by FEM-based unit cells, as function of the matrix volume fraction ($\xi^{(m)}$) in the three-phase system consisting of spherical TiN and AlN particles of equal size in a $Ti_{(1-x)}Al_xN$ matrix for four values of the Al mole fraction, $x = 0.25$, $x = 0.50$, $x = 0.66$, $x = 0.75$. The solid black line indicates the packing limit for spheres of identical size.

Figures 4.2.6, 4.2.7, 4.2.8 and 4.2.9 show the distribution of the strain energy W_e in one unit cell each of cases 1 to 4 after transformation. Different material properties of the phases (see table 3.1.1) and numbers of inclusions assigned to a given phase for each Al mole fraction, x, lead to different distributions of w_e.

Figure 4.2.6: Predicted distribution of the strain energy w_e after transformation evaluated for one unit cell of type UCSP, Al mole fraction $x = 0.25$, $\xi^{(m)} = 0.6$ and unconstrained conditions. The deformation scale factor is 21.576.
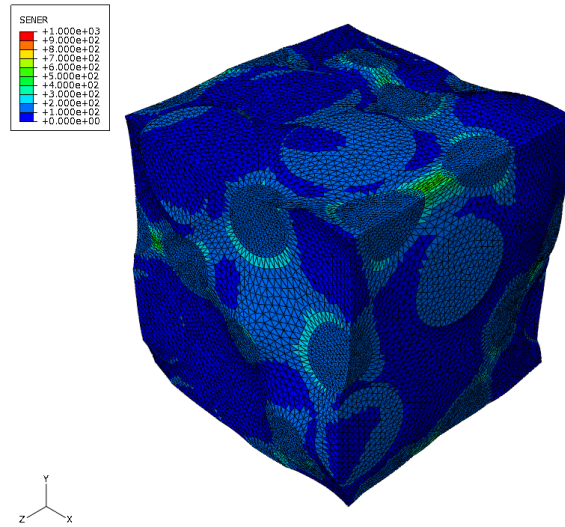
Figure 4.2.7: Predicted distribution of the strain energy w_e after transformation evaluated for one unit cell of type UCSP, Al mole fraction $x = 0.50$, $\xi^{(m)} = 0.6$ and unconstrained conditions. The deformation scale factor is 21.576.

Figure 4.2.8: Predicted distribution of the strain energy w_e after transformation evaluated for one unit cell of type UCSP, Al mole fraction $x = 0.66$, $\xi^{(m)} = 0.6$ and unconstrained conditions. The deformation scale factor is 21.576.
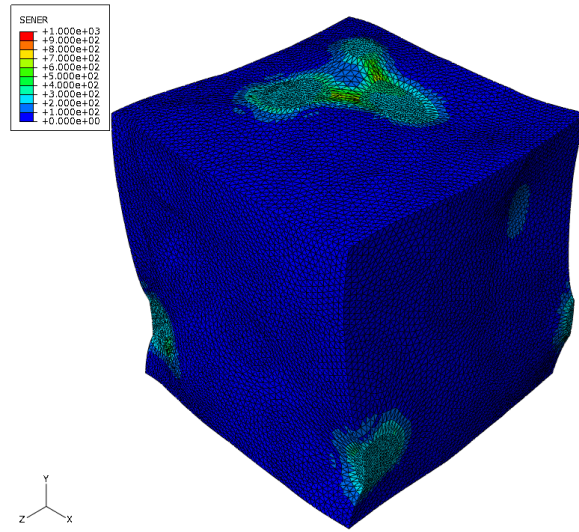

Figure 4.2.9: Predicted distribution of the strain energy w_e after transformation evaluated for one unit cell of type UCSP, Al mole fraction $x = 0.75$, $\xi^{(m)} = 0.6$ and unconstrained conditions. The deformation scale factor is 21.576.
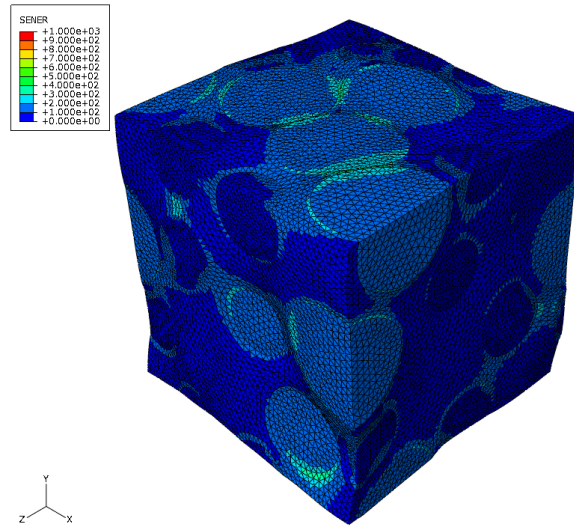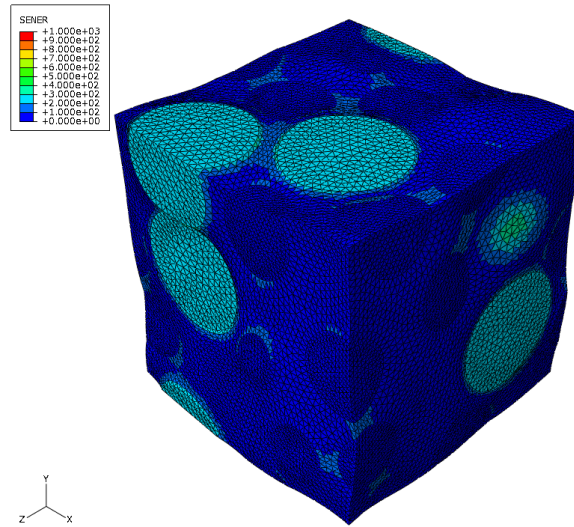
4.2.2 Influence of the Macroscopic Constraints on SED

Three macroscopic constraint conditions were applied to the unit cells of type USCP for Al mole fraction $x = 0.50$ and particle volume fraction $\xi^{(\mathrm{p})} = 0.4$. Table 4.2.2 presents results for $\overline{w_{\mathrm{e}}}$ for the unconstrained, fully constrained and layer constraint cases.

As expected, the highest values of $\overline{w_{\mathrm{e}}}$ are obtained for the fully constrained case ($\overline{w}_{\mathrm{e}}^{\mathrm{constr}} = 106.10\,\mathrm{MJ/m^3}$) because during transformation the unit cells' master nodes are not allowed to undergo any displacements (i.e., only local, periodic deformations of the cells' faces are allowed), leading to a buildup of stress and an increase in the internal energy and thus in the strain energy density. The lowest value is reached in the unconstrained case ($\overline{w}_{\mathrm{e}}^{\mathrm{unconstr}} = 102.76\,\mathrm{MJ/m^3}$) for the opposite reason: the unit cell is free to deform and no energy is needed to keep the faces restrained. Finally, the layer constraint case ($\overline{w}_{\mathrm{e}}^{\mathrm{layer\,constr}} = 104.24\,\mathrm{MJ/m^3}$) can be understood as a combination of above two cases, so it is logical to obtain an intermediate value.

Case	x	$\xi^{(\mathrm{p})}$	Mac. Constr.	UnitCell	$\overline{w_{\mathrm{e}}}$	Equation
[]	[]	[]	[]	[]	$\left[\mathrm{MJ/m^3}\right]$	[]
2	0.50	0.40	Unconstrained	UCSP	102.76	$\overline{w_{\mathrm{e}}} = 256.90\xi^{(\mathrm{p})}$
5	0.50	0.40	Fully Constrained	UCSP	106.10	$\overline{w_{\mathrm{e}}} = 265.25\xi^{(\mathrm{p})}$
6	0.50	0.40	Layer Constraint	UCSP	104.24	$\overline{w_{\mathrm{e}}} = 260.59\xi^{(\mathrm{p})}$

Table 4.2.2: List of $\overline{w_{\mathrm{e}}}$ results computed with the unit cell arrangement UCSP, for Al mole fraction $x = 0.50$, particle volume fraction $\xi^{(\mathrm{p})} = 0.4$ and different macroscopic constraints. Values for $\overline{w_{\mathrm{e}}}$ are averages from five different assignments of daughter phases to the particles.

Figure 4.2.10 shows the variation of $\overline{w_{\mathrm{e}}}$ as function of the matrix volume fraction, $\xi^{(\mathrm{m})}$, for the three macroscopic constraints considered. From this graphic a relationship between constraints and Al mole fraction (x) is obtained:

$$\overline{w}_{\mathrm{e}}^{\mathrm{fully\,constr}} > \overline{w}_{\mathrm{e}}^{\mathrm{layer\,constr}} > \overline{w}_{\mathrm{e}}^{\mathrm{unconstr}} \; \forall \; \xi^{(m)}, \, 0 \leq \xi^{(m)} \leq 1 \qquad . \qquad (4.2.2)$$

This relationship can be extended to the other cases were the Al mole fraction (x) is varied ($0 \leq x \leq 1$). Compared with the dependence of $\overline{w_{\mathrm{e}}}$ on the Al mole fraction, x, the macroscopic have less influence on $\overline{w_{\mathrm{e}}}$. The reason for this behavior is the relatively strong dependence of the material parameters on the Al mole fraction x.
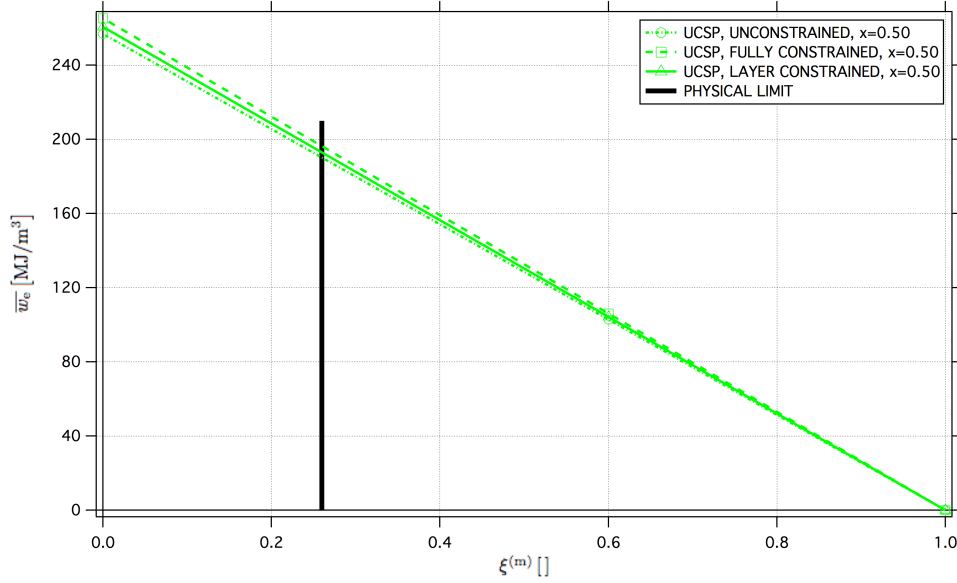
Figure 4.2.10: Strain energy density, calculated by FEM-based unit cells, for different macroscopic constraints, as function of the matrix volume fraction $\xi^{(m)}$ in the three-phase system consisting of spherical TiN and AlN particles in a $Ti_{0.5}Al_{0.5}N$ matrix. The solid black line indicates the packing limit for spheres of identical size.

4.2.3 Influence of the Elastic Contrast on SED

The elastic contrast (c_{el}) measures the level of inhomogeneity of the phases in a composite (see chapter 2.1.1). The elastic contrast of the cases under study was $0.99 \leqslant c_{el} \leqslant 1.05$, so it is very close to the "homogeneous value" of $c_{el} = 1$ for all cases. In order to understand the influence of this parameter on the behavior of materials with three transforming phases, five fictitious material property configurations were set up, see table 4.2.3. Again, five different assignments of the two particle phases to the 24 inhomogeneities of the cell were studied. The results were evaluated in terms of averages, standard deviations and coefficients of variation. The coefficient of variation, CV, is the relation between the standard deviation, θ, and the average of the samples, $\bar{\mu}$. It is useful when doing comparisons between data sets with widely different means.

$$CV = \frac{\theta}{\bar{\mu}}100 \tag{4.2.3}$$

Case 2 ($x = 0.50$, $\xi^{(m)} = 0.6$) is the basis of cases $2.a$ to $2.f$, where only the Young's moduli $E^{(TiN)}$ and $E^{(AlN)}$ of the inclusions are modified to fictitious values, whereas the rest of material parameters remain equal.

Case	c_{el}	$E^{(\mathrm{m})}$	$E^{(\mathrm{TiN})} = E^{(\mathrm{AlN})}$	$\theta(w_{\mathrm{e}})$	$\overline{w_{\mathrm{e}}}$	$CV(w_{\mathrm{e}})$
[]	[]	[GPa]	[GPa]	$\left[\mathrm{MJ/m^3}\right]$	$\left[\mathrm{MJ/m^3}\right]$	% []
2.a	0.01	387.00	3.87	0.00	2.30	0.02
2.b	0.1	387.00	38.70	0.37	20.07	0.19
2.c	1	387.00	387.00	0.00	102.14	0.00
2.d	10	387.00	3870.00	4.87	213.48	2.29
2.e	100	387.00	38700.00	8.20	250.39	3.28
2.f	1000	387.00	387000.00	8.70	255.22	3.41

Table 4.2.3: List of results computed from the unit cell arrangement UCSP, for Al mole fraction $x = 0.50$, $\xi^{(\mathrm{m})} = 0.6$ and unconstrained conditions for different fictitious values of the elastic contrast c_{el} values. The averages $\overline{w_{\mathrm{e}}}$, standard deviations $\overline{w_{\mathrm{e}}}$ and coefficients of variation $CV(w_{\mathrm{e}})$ pertain to five different assignments of the daughter phases to the particles.

The elastic contrasts c_{el} follow a logarithmic scale, from 0.01 to 1000. In cases 2.a and 2.f, the change in $CV(w_{\mathrm{e}})$ compared with the following or previous case is very small. Here, $CV(w_{\mathrm{e}})$ has an asymptotic behaviour, see figure 4.2.11. Case 2.c represents the particular case of an elastically homogeneous material.

The results for $CV(w_{\mathrm{e}})$ show that the elastic contrast has only a very limited influence on the standard deviation $\theta(w_{\mathrm{e}})$ of ensembles of the samples.

For high elastic contrasts the strain energy density tends towards an asymptotic value of about $255.22\,\mathrm{MJ/m^3}$, see figure 4.2.12. This behaviour is due to the high Young's moduli $E^{(\mathrm{p})}$ of the transforming inclusions which are embedded in a much softer matrix.
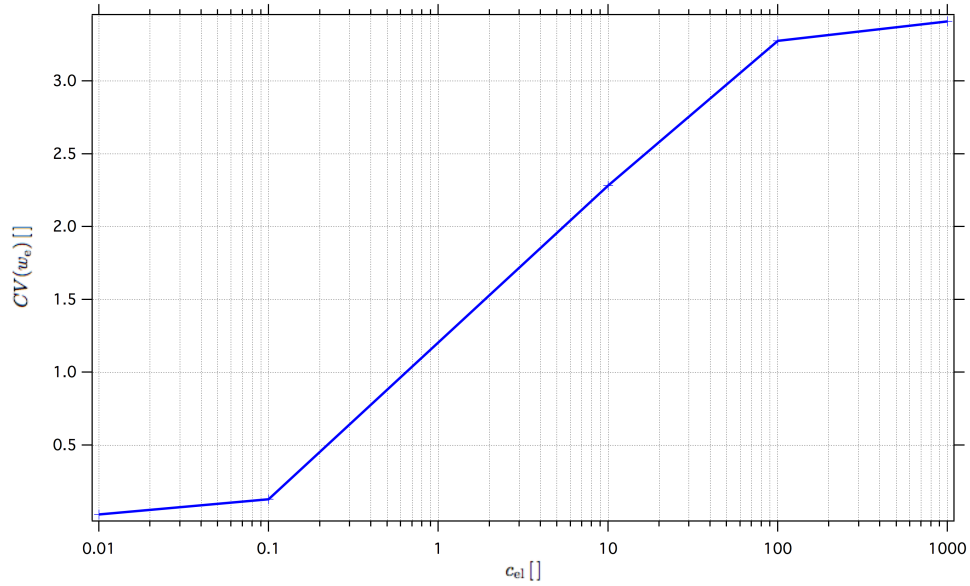
Figure 4.2.11: Coefficient of variation $CV(w_e)$ as function of the elastic contrast (c_{el}) in the three-phase system consisting of spherical TiN and AlN particles in a $Ti_{0.5}Al_{0.5}N$ matrix (UCSP arrangement, $\xi^{(p)} = 0.4$).

Figure 4.2.12: Strain energy density, calculated by FEM-based unit cells, as function of the elastic contrast (c_{el}) in the three-phase system consisting of spherical TiN and AlN particles in a $Ti_{0.5}Al_{0.5}N$ matrix (UCSP arrangement, $\xi^{(p)} = 0.4$).
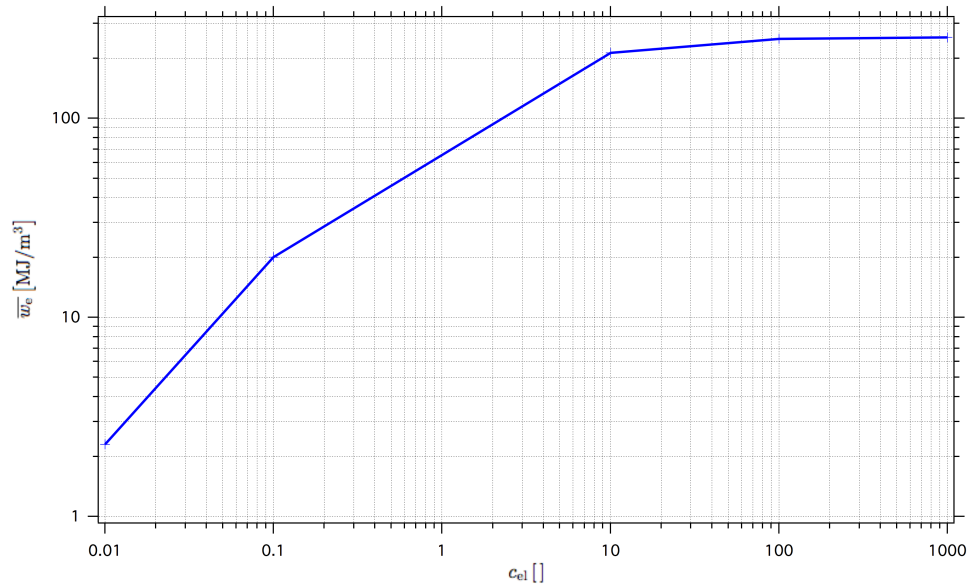
4.2.4 Influence of the Particle Shape on SED

Three particle shapes were employed in the cases 2, 7 and 8: randomly oriented spherical, cubic and tetrahedral particles. Table 4.2.4 shows the results for these cases. It is important to notice that the results for $\overline{w_\text{e}}$ of cases 7 and 8 cannot be compared directly with case 2 because they pertain to different values of $\xi^{(\text{p})}$. This problem can be circumvented by comparing the linear functions $\overline{w_\text{e}}(\xi^{(\text{p})})$. As can be seen in figure 4.2.13 the three inclusion shapes lead to a similar, but not equal, dependences between $\overline{w_\text{e}}$ and $\xi^{(\text{m})}$. Spherical particles can be seen to lead to the lowest and cube-shaped ones to the highest predicted values of the SED, the difference between them being about 1%.

Case	x	$\xi^{(\text{p})}$	Mac. Constr.	UnitCell	$\overline{w_\text{e}}$ $\left[\text{MJ/m}^3\right]$	Equation
[]	[]	[]	[]	[]		[]
2	0.50	0.40	Unconstrained	UCSP	102.76	$\overline{w_\text{e}} = 256.90\xi^{(\text{p})}$
7	0.50	0.20	Unconstrained	UCCP	51.89	$\overline{w_\text{e}} = 259.49\xi^{(\text{p})}$
8	0.50	0.20	Unconstrained	UCTP	51.84	$\overline{w_\text{e}} = 259.23\xi^{(\text{p})}$

Table 4.2.4: List of $\overline{w_\text{e}}$ results computed for different combinations of particle volume fraction, $\xi^{(\text{p})}$, and unit cell arrangements. Values for $\overline{w_\text{e}}$ are averages from five different assignments of daughter phases to the particles.
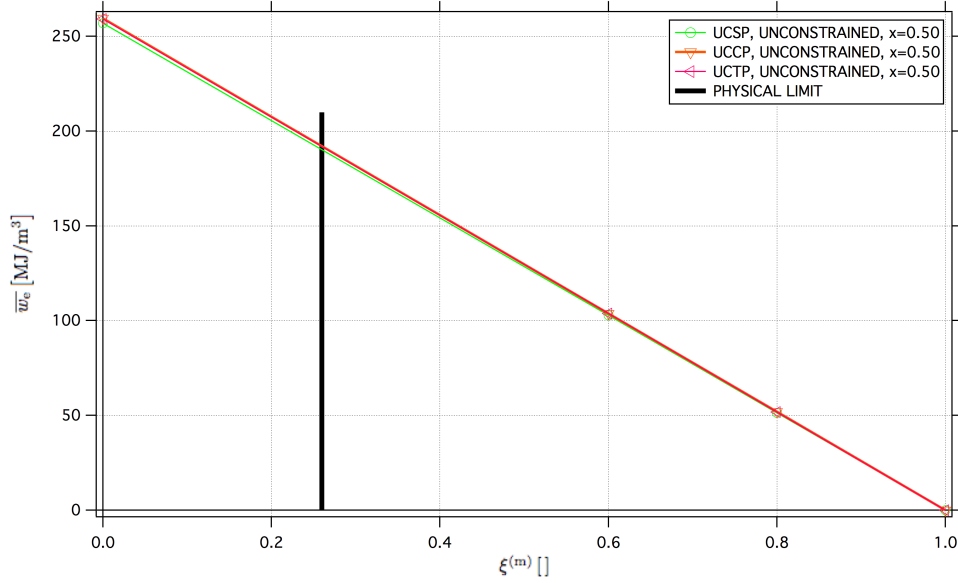
Figure 4.2.13: Strain energy density, calculated by FEM-based unit cells, for different inclusion shapes, as function of the matrix volume fraction $\xi^{(m)}$ in the three-phase system consisting of TiN and AlN particles in a $Ti_{0.5}Al_{0.5}N$ matrix. The solid black line indicates the packing limit for spherical inclusions of identical size.

The small difference between case 2 and cases 7 and 8 is due to the strain concentrations at the edges and corners of the cubic and tetrahedral particles, which induce an increase of $\overline{w_e}$ [20]. Figure 4.2.14 shows the deformed shapes of selected spherical, cube-shaped and tetrahedral inclusions. In addition, fringes of the maximum principal strain are plotted to highlight the concentrations of strain at the edges of the polyhedral inclusion shapes.

The clear deviation of the deformed shapes of the particles from arrangement UCSP from their original spherical shape is due to the influence of neighboring transformed inclusions; it is, of course, exaggerated due to the selected deformation scaling. The differences in size between the three different particles of a given composition (TiN and AlN) are due to the same reasons.
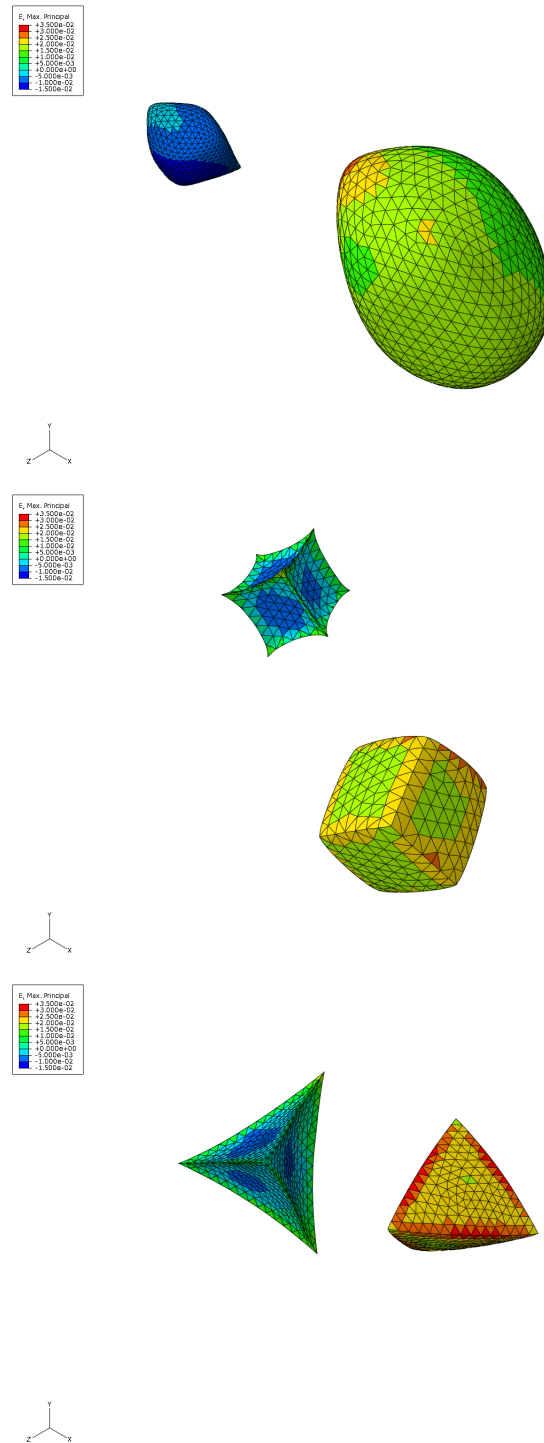
Figure 4.2.14: Predicted distributions of the maximum principal strain on selected TiN and AlN inclusions of the unit cell arrangements UCSP (top), UCCP (middle) and UCTP (bottom) after transformation, for Al mole fraction $x = 0.50$ and unconstrained conditions. The deformation scale factor is 21.576 for all particles shown.

4.2.5 Influence of the Microtopology on SED

Two unit cell topologies were studied: matrix inclusion-topologies and random topologies. Case 2 (spherical particles) is taken as a representative sample that defines the matrix-inclusion behaviour and is compared with cases 9, 10 and 11. Results for $\overline{w_e}$ are presented in table 4.2.5 as well as the equations that define the variation of $\overline{w_e}$ with $\xi^{(p)}$.

Case	x	$\xi^{(p)}$	Mac. Constr.	UnitCell	$\overline{w_e}$	Equation
[]	[]	[]	[]	[]	$[\text{MJ/m}^3]$	[]
2	0.50	0.40	Unconstrained	UCSP	102.76	$\overline{w_e} = 256.90\xi^{(p)}$
9	0.50	0.50	Unconstrained	UCRT	150.63	$\overline{w_e} = 301.27\xi^{(p)}$
10	0.50	0.66	Unconstrained	UCRT	199.98	$\overline{w_e} = 300.02\xi^{(p)}$
11	0.50	0.90	Unconstrained	UCRT	268.54	$\overline{w_e} = 298.38\xi^{(p)}$

Table 4.2.5: List of results for $\overline{w_e}$ computed for different combinations of particle volume fraction $\xi^{(p)}$ and unit cell arrangements. Values for $\overline{w_e}$ are averages from five different assignments of daughter phases to the particles.

As discussed in section 3.2.3 random microstructures were studied for three sets of phase volume fractions, five realizations being used in each case. Even though the three sets of unit cells show different microtopologies, the pertinent values of SED, while being distinctly higher than those of the "classical" matrix-inclusion topologies, can be very well described by a linear function of $\xi^{(m)}$, see figure 4.2.16. This result is difficult to interpret. If $\overline{w_e}$ showed a marked dependence on the microtopology, as indicated by the difference between the predictions of the UCSP and UCRP unit cells in figure 4.2.16, the results for the UCRP cases would not be expected to lie on one line. The most plausible explanation is that for loading exclusively by transformation strains, the stress and strain concentrations inherently present at the edges and vertices of phase regions composed of cube-shaped voxels lead to overestimating the SED. In addition, the voxel-based FE-mesh may not be sufficiently fine. Note that voxel models subjected to mechanical loading were not reported to show such clear effects of ragged phase boundaries [12, 27, 32, 37].

Figure 4.2.15 shows the variation of the SED at the surface of one unit cell of case 10. This plot is qualitatively different from figures 4.2.6 to 4.2.9 in being dominated by high-frequency fluctuations of the SED.
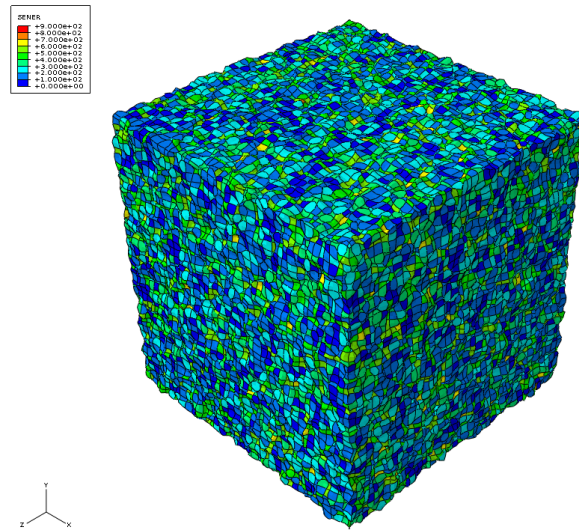
Figure 4.2.15: Predicted distribution of the strain energy W_e after transformation evaluated for one unit cell of type UCRT, Al mole fraction $x = 0.50$, $\xi^{(m)} = 0.33$ and unconstrained conditions. The deformation scale factor is 31.068.
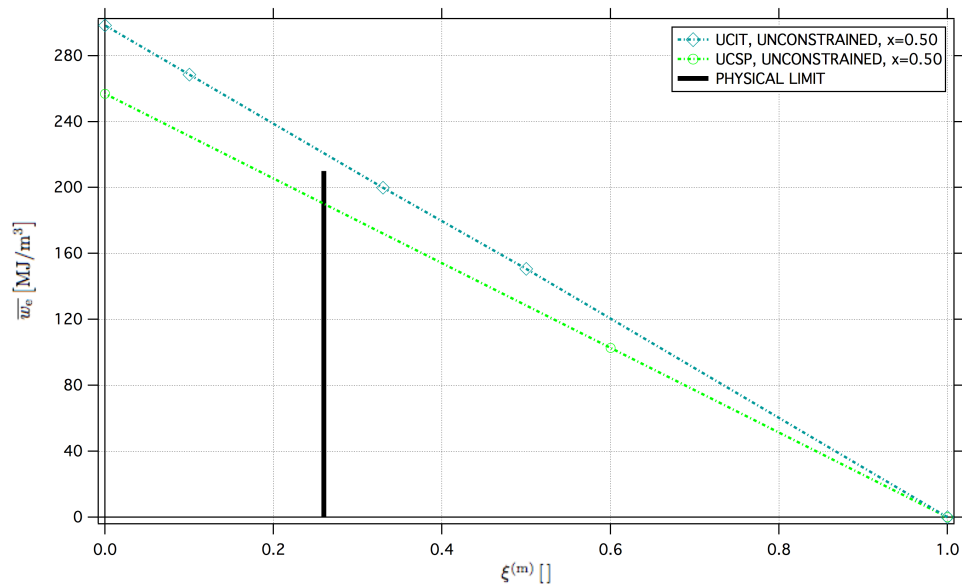

Figure 4.2.16: Strain energy density, calculated by FEM-based unit cells, as function of the parent phase volume fraction $\xi^{(m)}$ in the three-phase system consisting of TiN, AlN and $Ti_{0.5}Al_{0.5}N$ phases for different microtopology arrangements. The solid black line indicates the packing limit for spherical inclusions of identical size.

4.3 Comparison of FEM and TFA Results

It is important to stress that the main goal of this thesis is not only to understand how some factors affect the SED; in the background there is a second goal: to compare the results obtained using a finite element unit cell method with the analytical results calculated with the transformation field analysis. Analytical methods have less computational cost and the time required to perform the analysis is also much lower than the one needed by discretizing "full field" micromechanical methods.

The following figures show the graphics where $\overline{w_e}$ results, obtained with TFA, see figure 4.3.1, and FEM, see figure 4.3.2, are plotted as functions of $\xi^{(m)}$ for different configurations.
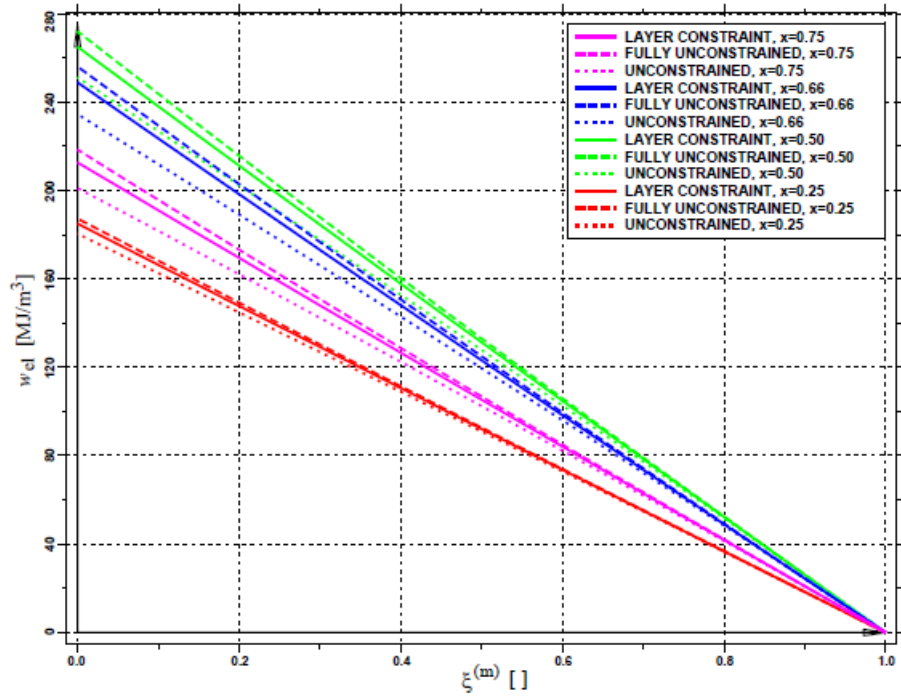

Figure 4.3.1: Strain energy density, calculated with TFA, as function of the matrix volume fraction $\xi^{(m)}$ in the three-phase system consisting of spherical TiN and AlN particles in a $Ti_{(1-x)}Al_xN$ matrix for four values of the Al mole fraction, $x = 0.25$, $x = 0.50$, $x = 0.66$, $x = 0.75$ [5].

Figure 4.3.2: Strain energy density, calculated by FEM-based unit cells, as function of the matrix volume fraction $\xi^{(m)}$ in the three-phase system (UCSP) consisting of spherical TiN and AlN particles in a $\mathrm{Ti}_{(1-x)}\mathrm{Al}_x\mathrm{N}$ matrix for four values of the Al mole fraction, $x = 0.25$, $x = 0.50$, $x = 0.66$, $x = 0.75$. The solid black line indicates the packing limit for spherical inclusions of identical size.

In order to compare the previous graphics, the relative difference between $\overline{w}_{e,\mathrm{FEM}}$ and $w_{e,\mathrm{TFA}}$ is evaluated as

$$\Delta = \frac{|\overline{w}_{e,\mathrm{FEM}} - w_{e,\mathrm{TFA}}|}{\overline{w}_{e,\mathrm{FEM}}} 100 \qquad , \tag{4.3.1}$$

and plotted.

Case	x	$\xi^{(\mathrm{p})}$	Mac. Constr.	UnitCell	$\overline{w}_{\mathrm{e,FEM}}$	$w_{\mathrm{e,M-TFA}}$	$w_{\mathrm{e,S-TFA}}$	Δ
[]	[]	[]		[]	$\left[\mathrm{MJ/m^3}\right]$	$\left[\mathrm{MJ/m^3}\right]$	$\left[\mathrm{MJ/m^3}\right]$	% []
1	0.25	0.40	Unconstrained	UCSP	72.93	72.86	−	0.09
2	0.50	0.40	Unconstrained	UCSP	102.76	102.59	−	0.17
3	0.66	0.40	Unconstrained	UCSP	96.19	96.02	−	0.17
4	0.75	0.40	Unconstrained	UCSP	82.38	82.24	−	0.17
5	0.50	0.40	Fully Constrained	UCSP	106.10	105.93	−	0.16
6	0.50	0.40	Layer Constraint	UCSP	104.24	104.08	−	0.15
9	0.50	0.50	Unconstrained	UCRT	150.63	127.78	128.17	15.2
10	0.50	0.66	Unconstrained	UCRT	199.98	170.18	171.59	14.9
11	0.50	0.90	Unconstrained	UCRT	268.54	226.72	229.23	15.6

Table 4.3.1: List of predictions for $\overline{w}_{\mathrm{e}}$ computed with the FEM and TFA based on Mori-Tanaka and classical self consistent methods for different combinations of Al mole fractions, x, particle volume fraction, $\xi^{(\mathrm{p})}$, macroscopic constraints and unit cell arrangements.

The TFA results for $w_{\mathrm{e,M-TFA}}$, TFA based on Mori-Tanaka method, obtained in cases 1 to 6 are extremely close to the corresponding predictions obtained by FE-based unit cells with matrix-inclusion topology, $\overline{w}_{\mathrm{e,FEM}}$. As can be seen in figures 4.3.3 and 4.3.4, the relative differences are of the order of $\Delta = 0.17\%$. The TFA based on the Mori-Tanaka method gives accurate $\overline{w}_{\mathrm{e}}$ results in modeling a low-contrast three-phase system material consisting of equiaxed particles embedded in a matrix for different macroscopic constraints.

The predictions of the SED for the random microstructures, cases 9 to 11, which cover different microtopologies, differ clearly from the results obtained with the TFA based on Mori-Tanaka ($w_{\mathrm{e,M-TFA}}$) and self-consistent ($w_{\mathrm{e,S-TFA}}$) schemes, compare table 4.3.1, Δ being two orders of magnitude higher for cases 9 to 11 than for cases 1 to 8. As noted in section 4.2.5 this discrepancy is not well understood at present, but may be due to effects of the ragged phase boundaries of the voxel models.

Figure 4.3.3: Values of Δ in the three-phase system consisting of spherical TiN and AlN particles in a $Ti_{(1-x)}Al_xN$ matrix for four values of the Al mole fraction, $x = 0.25$, $x = 0.50$, $x = 0.66$, $x = 0.75$ and unconstrained conditions.
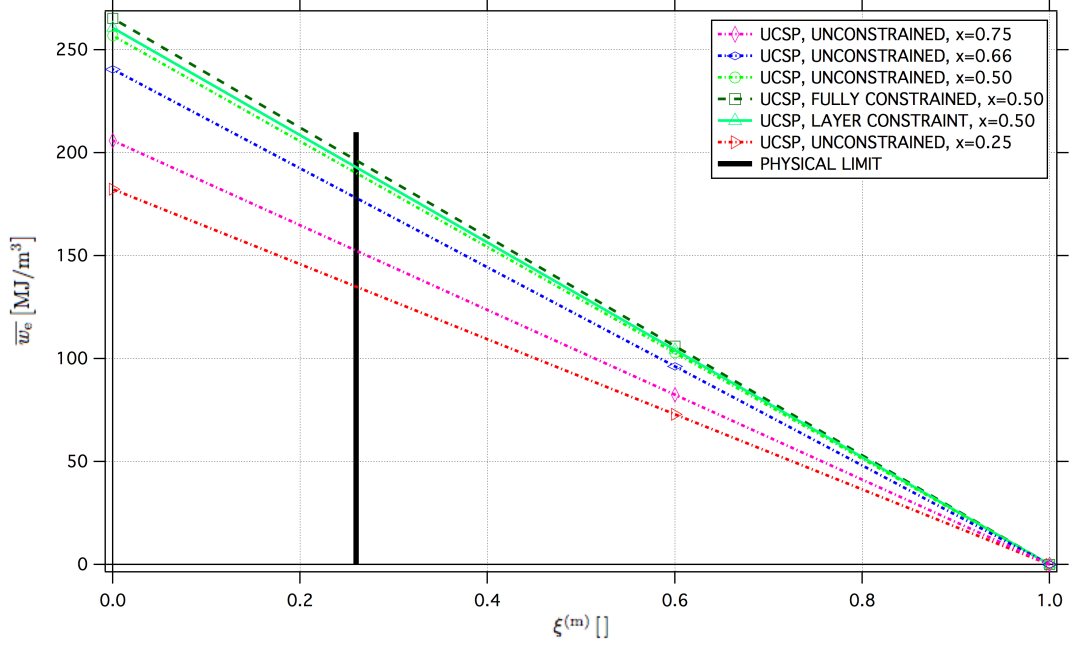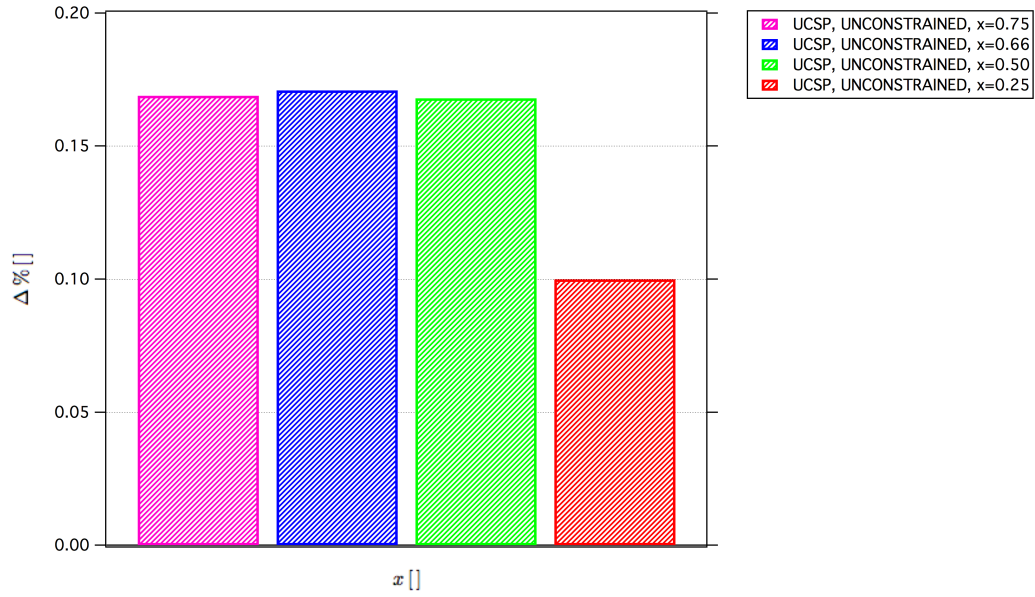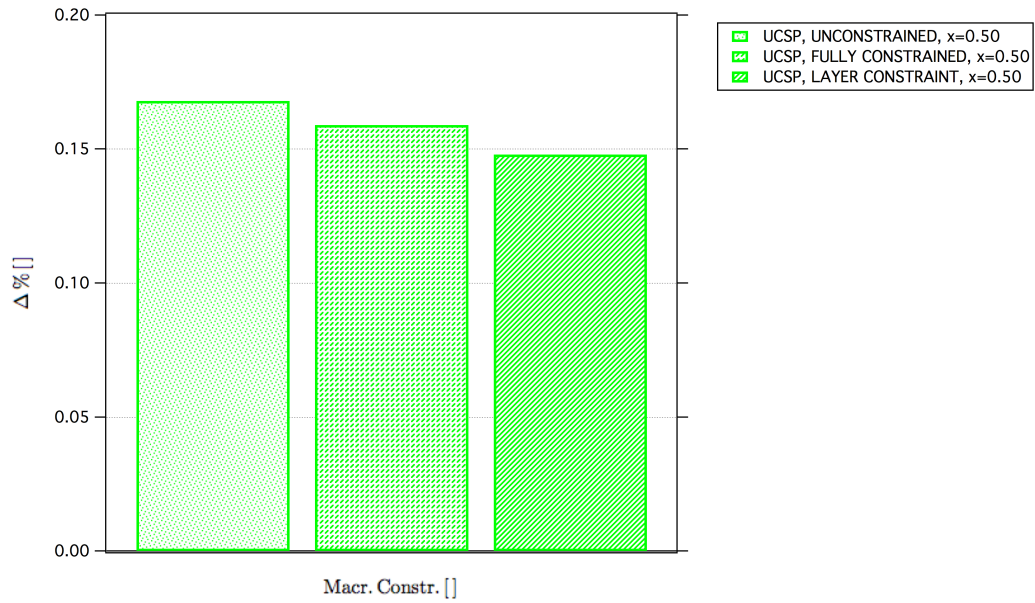

Figure 4.3.4: Values of Δ in the three-phase system consisting of spherical TiN and AlN particles in a $Ti_{0.5}Al_{0.5}N$ matrix for unconstrained, fully constrained and layer constraint conditions.

The different elastic contrast cases, 2.a to 2.f, were also evaluated with the TFA based on the Mori-Tanaka method. On the one hand, for a low elastic contrast (cases 2.a and 2.b) the relative differences to the unit cell results are almost zero, see figure 4.3.5. The TFA method cannot be used for case 2.c because it is an homogeneous model: matrix and particles have the same Young's modulus, see table 4.2.3. On the other hand, for high elastic contrast cases, 2.d to 2.f, there is a considerable difference between the SED results predicted by the two methods, see figure 4.3.5. The main reason of this behaviour is the influence of details of the microstructure on the physical system, which become more dominant for high c_{el} values.

Case	c_{el}	x	$\xi^{(\mathrm{p})}$	Mac. Constr.	UnitCell	$\overline{w}_{\mathrm{e,FEM}}$	$w_{\mathrm{e,M-TFA}}$	Δ
[]	[]	[]	[]	[]	[]	$\left[\mathrm{MJ/m^3}\right]$	[]	% []
2.a	0.01	0.50	0.40	Unconstrained	UCSP	2.30	2.29	0.43
2.b	0.1	0.50	0.40	Unconstrained	UCSP	20.07	20.68	3.04
2.c	1	0.50	0.40	Unconstrained	UCSP	102.14	–	–
2.d	10	0.50	0.40	Unconstrained	UCSP	213.48	169.29	20.70
2.e	100	0.50	0.40	Unconstrained	UCSP	250.39	181.25	27.61
2.f	1000	0.50	0.40	Unconstrained	UCSP	255.22	182.54	28.41

Table 4.3.2: List of predictions for $\overline{w}_{\mathrm{e}}$ results computed with unit cell and TFA methods for different values of the elastic contrast.
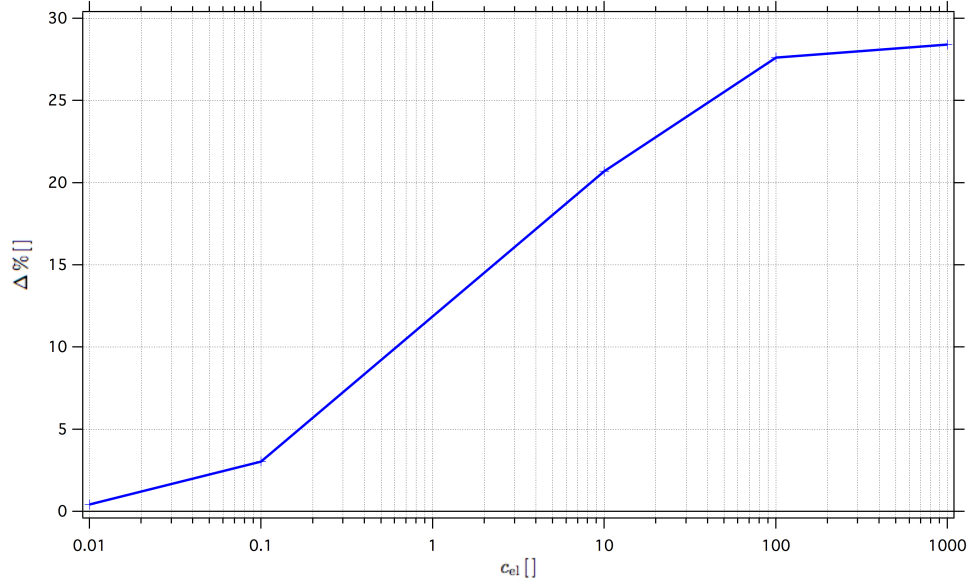
Figure 4.3.5: Values of Δ in the three-phase system consisting of spherical TiN and AlN particles in a $\text{Ti}_{(1-x)}\text{Al}_x\text{N}$ matrix for different values of the elastic contrast, $c_{\text{el}} = 0.01$, $c_{\text{el}} = 0.1$, $c_{\text{el}} = 10$, $c_{\text{el}} = 100$, $c_{\text{el}} = 1000$, a value of the Al mole fraction $x = 0.50$, and unconstrained conditions.

Accordingly, the surprisingly good agreement between TFA based on the Mori-Tanaka method and unit cell models for matrix-inclusion topologies evident in table 4.3.1 and figure 4.3.3 is to a considerable extent due to the low elastic contrast of the TiN-AlN-TiAlN system. In this low contrast regime the TFA gives excellent predictions for matrix-inclusion topologies and reasonable approximations for random microtopologies.

5 Conclusions

In the present work the strain energy densities of transforming ternary hard layers are evaluated within the framework of continuum micromechanics of inhomogeneous media.

Transformation field analysis in combination with the Mori-Tanaka and classical self consistent methods was employed to obtain analytical predictions for the SED and compare them with results obtained by a FE-based unit cell method.

Following a procedure, developed in previous studies, for generating periodic unit cell arrangements that contain a fixed number of inclusions of equal size, different configurations with constant ratio of matrix volume and particle volumes were generated and evaluated.

The SED results obtained with the TFA method agree well with those generated by multi-particle unit cells for three-phase systems with matrix-inclusion topology and elastic contrast close to unity. However, when the elastic contrast takes high values, the disagreement between the TFA and the FE-based unit cell method increases to nearly 30%. Voxel-type unit cells describing three-phase random materials give predictions for the SED that exceed the corresponding TFA results by approximately 15%.

It can be concluded that the TFA provides accurate predictions for the SED of three-phase systems consisting of a matrix of the parent phase plus inclusions transforming into the daughter phases with elastic contrast close to unity. Variations in macroscopic constraints, shape and distribution have little influence on the SED of such systems.

Future work could use realistic arrangements of the TiN-AlN-TiAlN system instead of random topologies. Accordingly, predictions computed with the FEM would be more accurate and closer to the real behaviour of the system.

Bibliography

[1] ABAQUS. *Rev.6.9 User's Manual*. HKS Inc., Pawtucket, RI, 2010.

[2] Y. Benveniste. A new approach to the application of Mori–Tanaka's theory in composite materials. *Mech. Mater.*, 6:147–157, 1987.

[3] J.Y. Buffière, P. Cloetens, W. Ludwig, E. Maire, and L. Salvo. In situ X-ray tomography studies of microstructural evolution combined with 3D modeling. *MRS Bull.*, 33:611–619, 2008.

[4] H.J. Böhm. A short introduction to continuum micromechanics. ILSB Report 206, Institute of Lightweight Design and Structural Biomechanics, TU Vienna, 2004.

[5] H.J. Böhm. Stress and strain fields due to multiple transforming inhomogeneities. ILSB Report 190, Institute of Lightweight Design and Structural Biomechanics, TU Vienna, 2008.

[6] H.J. Böhm, and W. Han. Comparisons between three-dimensional and two-dimensional multi-particle unit cell models for particle reinforced metal matrix composites. *Modell. Simul. Mater. Sci. Engng.*, 9:47–65, 2001.

[7] W.J. Drugan, and J.R. Willis. A micromechanics-based nonlocal constitutive equation and estimates of the representative volume element size for elastic composites. *J. Mech. Phys. Solids* 44, 497–524, 1996.

[8] G.J. Dvorak, and Y. Benveniste. On transformation strains and uniform fields in multiphase elastic media. *Proc. Math. and Phys. Sciences.*, 437:291-310, 1992.

[9] J.D. Eshelby. The determination of the elastic field of an ellipsoidal inclusion and related problems. *Proc. Roy. Soc. London*, A241:376–396, 1957.

[10] H.F. Fischmeister, and B. Karlsson. Plastizitätseigenschaften grob-zweiphasiger Werkstoffe. *Z. Metallkd.*, 68:311–327, 1977.

[11] S. Ghosh, K.H. Lee, and S. Moorthy. Two scale analysis of heterogeneous elastic-plastic materials with asymptotic homogenization and Voronoi cell finite element model. *Comput. Meth. Appl. Mech. Engng.*, 132:63–116, 1996.

[12] R.E. Guldberg, S.J. Hollister, and G.T. Charras. The accuracy of digital image-based finite element models. *J. Biomech. Engng.*, 120:289–295, 1998.

[13] A.A. Gusev. Representative volume element size for elastic composites: a numerical study. *J. Mech. Phys. Solids* 45, 1449–1459, 1997.

[14] R. Hill. A self-consistent mechanics of composite materials. *J. Mech. Phys. Sol.*, 13:213–222, 1965b.

[15] R. Hill. The essential structure of constitutive laws for metal composites and polycrystals. *J. Mech. Phys. Sol.*, 15:79–95, 1967.

[16] A. Hölinga, L. Hultman, M. Odén, J. Sjölén, and L. Karlsson. Mechanical properties and machining performance of $Ti_{(1-x)}Al_xN$-coated cutting tools. *Surf. & Coat. Tech.*, 191:384–392, 2005.

[17] HYPERMESH. *Rev10.0 User's Manual.* Altair Engineering Inc., Troy, MI, *2010.*

[18] Jožef Stefan Institute. Hard coatings. 2010. URL: *http://www.ijs.si.*

[19] K. Kutschej, P.H. Mayrhofer, M. Kathrein, P. Polcik, R. Tessadri, and C. Mitterer. Structure, mechanical and tribological properties of sputtered $Ti_{(1-x)}Al_xN$ coatings with $0.5 \leq x \leq 0.75$. *Surf. & Coat. Tech.*, 200:2358–2365, 2005.

[20] Y. Li, and K.T. Ramesh. Influence of particle volume fraction, shape, and aspect ratio on the behavior of particle-reinforced metal-matrix composites at high rates of strain. *Acta mater.*, 46:5633-5646, 1998.

[21] J. Llorca, and J. Segurado. Three-dimensional multiparticle cell simulations of deformation and damage in sphere-reinforced composites. *Mater Sci. Eng. A*, 365:267–274, 2004.

[22] P.H. Mayrhofer. Private comunication. MontanUniversität Leoben, Leoben, Austria, 2010.

[23] P.H. Mayrhofer, F. D. Fischer, H. J. Böhm, C. Mitterer, and J. M. Schneider. Energetic balance and kinetics for the decomposition of supersaturated $Ti_{(1-x)}Al_xN$. *Acta Mater.*, 55:1441-1446, 2007.

[24] P.H. Mayrhofer, D. Music, and J. M. Schneider. Influence of the Al distribution on the structure, elastic properties, and phase stability of supersaturated $Ti_{(1-x)}Al_xN$. *J. Appl. Phys.* 100:094906, 2006.

[25] T. Mori, and K. Tanaka. Average stress in the matrix and average elastic energy of materials with misfitting inclusions. *Acta Metall.*, 21:571–574, 1973.

[26] T. Mura. Micromechanics of defects in solids. Martinus Nijhoff, Dordrecht, 1987.

[27] G.L. Niebur, J.C. Yuen, A.C. Hsia, and T.M. Keaveny. Convergence behavior of high-resolution finite element models of trabecular bone. *J. Biomech. Engng.*, 121:629–635, 1999.

[28] S. Nogales. Numerical simulation of the thermal and thermomechanical behaviour of metal matrix composites. Doctoral Thesis, TU Vienna, Vienna, Austria, 2008.

[29] D.H. Pahr, and H.J. Böhm. Assessment of mixed uniform boundary conditions for predicting the mechanical behavior of elastic and inelastic discontinuously reinforced composites. *Comput. Model. Engng. Sci.*, 34:117–136, 2008.

[30] PYTHON. *Rev.2.6 User's Manual. 2010.*

[31] A. Rasool. Improved multi-particle unit cell models for studying particle reinforced composites. Doctoral Thesis, TU Vienna, Vienna, Austria, 2011.

[32] A.P. Roberts, and E.J. Garboczi. Elastic properties of a tungsten–silver composite by reconstruction and computation. *J. Mech. Phys. Sol.*, 47:2029–2055, 1999.

[33] S. Schmauder, J. Wulf, T. Steinkopff, and H. Fischmeister. Micromechanics of plasticity and damage in an Al/SiC metal matrix composite. In A. Pineau and A. Zaoui, editors, *Micromechanics of Plasticity and Damage of Multiphase Materials*, pages 255–262, Dordrecht, 1996. Kluwer.

[34] J. Segurado. Micromecánica computacional de materiales compuestos reforzados con partículas. Doctoral Thesis, Universidad Politécnica de Madrid, Madrid, Spain, 2004.

[35] J. Segurado, and J. Llorca. A numerical approximation to the elastic properties of sphere-reinforced composites. *J. Mech. Phys. Solids*, 50:2107–2121, 2002.

[36] J. Segurado, and J. Llorca. Computational micromechanics of composites: The effect of particle spatial distribution. *Mech. Mate*r., 38:873–883, 2006.

[37] K. Terada, T. Miura, and N. Kikuchi. Digital image-based modeling applied to the homogenization analysis of composite materials. *Comput. Mech.*, 20:331–346, 1997.

[38] S. Torquato. Morphology and effective properties of disordered heterogeneous media. *Int. J. Sol. Struct.*, 35:2385–2406, 1998.

[39] Z.H. Xia, W.A. Curtin, and P.W.M. Peters. Multiscale modeling of failure in metal matrix composites. *Acta mater.*, 49:273–287, 2001.

[40] J. Zeman, and M. Šejnoha. Numerical evaluation of effective elastic properties of graphite fiber tow impregnated by polymer matrix. *J. Mech. Phys. Sol.*, 49:69–90, 2001.

[41] T.I. Zohdi. A model for simulating the deterioration of structural-scale material responses of microheterogeneous solids. In D. Gross, F. D. Fischer, and E. van der Giessen, editors, *Euromech Colloqium 402 — Micromechanics of Fracture Processes*, pages 91–92, Darmstadt, 1999. TU Darmstadt.